



UNIVERSITÀ DI PISA  
DOTTORATO DI RICERCA IN INGEGNERIA DELL'INFORMAZIONE

# NOVEL SIGNAL PROCESSING TECHNIQUES FOR THE EXPLOITATION OF THERMAL HYPERSPECTRAL DATA

DOCTORAL THESIS

Author  
**Matteo Moscadelli**

Tutor (s)

**Prof. Marco Diani, Prof. Giovanni Corsini**

Reviewer (s)

**Prof. Andrea Garzelli, Dr. Ingebjørg Kåsen**

The Coordinator of the PhD Program

**Prof. Fulvio Gini**

Pisa, November 2019

XXXII



To my family and Elisa...



"If you want to find the secrets of the Universe,  
think in terms of energy, frequency and vibration."  
Nikola Tesla



---

---

## Summary

---

**T**HIS doctoral thesis attempts to propose a novel signal processing chain, aimed to exploit data acquired by long wave infrared (LWIR) hyperspectral sensors. In the LWIR, infrared radiation from an object is directly related to its temperature, i.e. hotter the surface, higher the emitted thermal energy. Hyperspectral sensors capture the radiated energy from the objects (target) in a large number of consecutive spectral bands within the LWIR, e.g. with the aid of a prism, in order to estimate the spectrum (spectral emissivity) and the temperature of the surface material.

In this framework, two main challenging tasks affect the development and the deployment of thermal hyperspectral sensors:

- *atmospheric correction*: the process of estimate and compensate the thermal radiation produced by the atmosphere, that affects the thermal radiation produced by the target. This process is made more complicated by the complex combination of atmospheric parameters, such as temperature, pressure, water vapor concentration, aerosol concentration etc., and by the complex profile that such a parameters follow from ground towards the space, passing through all the atmospheric layers.
- *temperature emissivity separation*: often abbreviated as *TES problem*; once the atmospheric correction of the signal has been applied, it represents the task of jointly estimate the surface spectral emissivity and temperature of the observed target. The estimate represents an ill-posed problem: given the thermal radiation of the target, measured at  $N_c$  different channels of the deployed hyperspectral sensor, the unknowns of the problem are  $N_c + 1$ , i.e. the  $N_c$  spectral sample of its emissivity, and the temperature.

In this framework, the thesis aim to provide a processing chain for the exploitation of the thermal radiation, captured by hyperspectral sensors, focused on the task of *target detection*, i.e. recognize a given material within a complex remote sensing scenario. The applications of such a signal processing chain may be the more disparate, from environmental remote sensing (climate change, volcanos monitoring, gas and waste pollution etc.) to defence and surveillance purposes.

---

## Outline

This thesis consists of four chapters:

1. **Introduction to LWIR Hyperspectral Imaging:** in the first chapter, an introduction to the framework of hyperspectral systems is provided. In particular, the first part concern an appropriate recap of what the LWIR hyperspectral remote sensing is. Then, a precise description regarding on how to represent an hyperspectral image is discussed. In particular, are highlighted and described the two main techniques, used by the modern sensors, to acquire the thermal radiation. At the end, the presentation of the signal model, commonly used by the scientific community, is provided and deeply described.
2. **Polynomial-fitting Temperature and Emissivity Separation:** in the second chapter, a new algorithm for Temperature-Emissivity Separation is presented. The simultaneous retrieval of both physical quantities from the measured radiance represents an ill-posed problem, because the target spectral signature and its temperature are jointly combined into the remotely-sensed signal. Furthermore, the atmospheric downwelling radiance and the surface-emitted radiance are also coupled together through the emissivity, making the estimation even more complicated. In the first part, a known atmosphere is assumed, and the proposed algorithm solves the TES indeterminateness exploiting an optimization procedure, by estimating the best temperature that minimizes the atmospherical-residuals features inside the emissivity spectral shape. The temperature is estimated within a small spectral interval where the emissivity is smooth. In order to measure the signature smoothness in several intervals, an erosion-moving average filtering procedure is applied to the ground leaving radiances. Such filtering allows to establish the smoother region where the algorithm produces better results in terms of emissivity polynomial fitting. In the second part, the atmosphere is supposed unknown. In order to accomplish the atmospheric correction, and further perform the TES task, a Look-up-Table (LUT) of plausible atmospheres is provided as input of the algorithm. The latter are obtained with the aid of the software MODTRAN, based on assumptions regarding the predicted atmosphere of the remote sensing scenario.
3. **Improved Alpha Residuals:** the third chapter presents a new method to compute alpha residuals (AR) in longwave infrared hyperspectral images. AR allow emissivity-based target detection being them a quantity, related to the target emissivity, which is less prone to errors in the estimated temperature. The proposed method improves existing approaches taking into account also the contribution of the atmospheric emitted radiance reflected by the object. Experimental results over synthetic data show the better performance of the new approach.
4. **Subspace-based Target Detection:** the fourth and last chapter presents a new method to detect materials with known spectral emissivity in data acquired by longwave infrared hyperspectral sensors. The proposed approach differs from existing methods because it takes into account the uncertainty of the downwelling radiance. Such uncertainty is addressed assuming that the downwelling radiance spans a low-rank subspace whose basis matrix is learned, regardless of the analyzed image, from MODTRAN simulated spectra. The analysis, carried out over

---

data simulated by considering different atmospheric conditions, surface temperatures, and emissivity spectra, shows the effectiveness of the proposed algorithm.



---

---

## List of publications

---

### International Journals

---

1. Diani, M., Moscadelli, M., and Corsini, G. (2018). Improved alpha residuals for target detection in thermal hyperspectral imaging. *IEEE Geoscience and Remote Sensing Letters*, 15(5), 779-783.
2. Acito, N., Moscadelli, M., Diani, M., and Corsini, G. (2018). Subspace-based Target Detection in LWIR Hyperspectral Imaging. *IEEE Geoscience and Remote Sensing Letters*, *Early Access Article*, DOI: 10.1109/LGRS.2019.2939751.

### International Conferences/Workshops with Peer Review

---

1. Brisken, S., Moscadelli, M., Seidel, V., and Schwark, C. (Seattle, May 2017). Passive radar imaging using DVB-S2. In *Proceedings of the 2017 IEEE Radar Conference (RadarConf)* (pp. 0552-0556). IEEE.
2. Moscadelli, M., Diani, M., and Corsini, G. (Jyvaskyla, October 2017). TEMPERATURE - EMISSIVITY SEPARATION ASSESSMENT IN A SUB-URBAN SCENARIO. *International Archives of the Photogrammetry, Remote Sensing and Spatial Information Sciences*, 42.
3. Moscadelli, M., Diani, M., Corsini, G., Riccobono, A. and Porta, A. (Amsterdam, September 2018). Polynomial-fitting temperature and emissivity separation in LWIR hyperspectral imaging. In *Proceedings of the 9<sup>th</sup> IEEE Workshop on Hyperspectral Imaging and Signal Processing: Evolution in Remote Sensing (WHISPERS)*, IEEE.
4. Moscadelli, M., Acito, N., Diani, M. and Corsini, G. (Firenze, September 2019). A novel method for LWIR hyperspectral target detection by means of a subspace-based approach. In *Proceedings of the 15<sup>th</sup> International Workshop on Advanced Infrared Technology and Applications (AITA)*.

---

## Others

---

1. Moscadelli, M. (Napoli, May 2017). Assessment of temperature and emissivity estimation methodologies in thermal hyperspectral imagery. In 1<sup>st</sup> Radar and Remote Sensing Workshop. *Gruppo Telecomunicazioni e Tecnologie dell'Informazione (GTTI)*.
2. Moscadelli, M. (Pavia, May 2018). Improved Alpha Residuals for Target Detection in Thermal Hyperspectral Imaging. In 2<sup>nd</sup> Radar and Remote Sensing Workshop. *Gruppo Telecomunicazioni e Tecnologie dell'Informazione (GTTI)*.
3. Moscadelli, M., Riccobono, A., Giunti, C., Guadagnoli, E. and Porta, A. (2018, September). Polynomial-fitting Temperature-Emissivity Separation in Thermal IR Hyperspectral Imagery. *Polaris Innovation Journal - Leonardo Spa Technical Review*. (Issue 35, pp. 25-31). Leonardo Spa.

---

---

# Contents

---

<b>Summary</b>	<b>III</b>
<b>1 Introduction to LWIR Hyperspectral Imaging</b>	<b>1</b>
1.1 Hyperspectral Remote Sensing . . . . .	1
1.2 Representation of Hyperspectral Images . . . . .	3
1.3 Signal Model . . . . .	4
<b>2 Polynomial-fitting Temperature and Emissivity Separation</b>	<b>7</b>
2.1 Introduction . . . . .	7
2.2 PTES algorithm . . . . .	9
2.2.1 Spectral Interval Selection . . . . .	11
2.2.2 Experimental Results . . . . .	12
2.3 PTES with Atmospheric Correction . . . . .	16
2.3.1 Analysis of the spectral window . . . . .	17
2.3.2 Experimental results . . . . .	19
2.3.3 Discussion . . . . .	20
2.4 Conclusions . . . . .	25
<b>3 Improved Alpha Residuals</b>	<b>26</b>
3.1 Introduction . . . . .	26
3.2 Problem Statement . . . . .	27
3.3 Improved Alpha Residuals . . . . .	29
3.4 Experimental Results . . . . .	32
3.4.1 Effectiveness of the orthogonal projection . . . . .	33
3.4.2 Analysis of the estimation accuracy . . . . .	33
3.5 Conclusions . . . . .	36
<b>4 Subspace-based Target Detection</b>	<b>39</b>
4.1 Introduction . . . . .	39
4.2 Algorithm Description . . . . .	40
4.2.1 Determination of the Basis Matrix $U$ . . . . .	42

## Contents

---

4.3 Simulation Strategy . . . . .	43
4.4 Experimental Results . . . . .	44
4.5 Conclusions . . . . .	49
<b>5 Conclusions of the Thesis</b>	<b>50</b>
<b>Bibliography</b>	<b>52</b>
<b>List of figures</b>	<b>54</b>
<b>List of tables</b>	<b>55</b>
<b>Formation Activities during the Years of PhD Program</b>	<b>57</b>
<b>Biography</b>	<b>58</b>

---

## Introduction to LWIR Hyperspectral Imaging

---

### 1.1 Hyperspectral Remote Sensing

---

The term *remote sensing* indicates the process of monitoring and acquisition of physical information about a target of interest (TOI, hereinafter), without physical contact. The physical characteristics of the target are acquired by measuring its reflected and/or emitted electromagnetic radiation at a distance from the object itself.

Remote sensing of a TOI can be performed with several sensors. The choice of the most suitable sensor depends on several aspects, such as the physical features of the target, the characteristics of the environment, and the available platform where the sensor is carried on. Generally, the remote sensing devices are split in two macro-categories:

- active devices, such as:
  - active radar
  - sonar (instead of electromagnetic radiation, in this case the sensor captures mechanical vibrations of a liquid or gas)
  - lidar (laser radar)
- passive devices, such as:
  - passive radar
  - electro-optical (EO) sensors

In the framework of passive systems, EO sensors are electronic detectors that convert light (visible or infrared photons) into an electrical signal. These devices are categorized based on the portion of the electromagnetic spectrum where they work:

- visible (VIS) cameras: radiation with wavelength from 0.4 to 0.7 $\mu m$

## Chapter 1. Introduction to LWIR Hyperspectral Imaging

- near infrared (NIR) cameras: radiation with wavelength from  $0.7$  to  $1.1\mu m$
- short-wave infrared (SWIR) cameras: radiation with wavelength from  $1.1$  to  $3\mu m$
- medium-wave infrared (MWIR) cameras: radiation with wavelength from  $3$  to  $5\mu m$
- long-wave infrared (LWIR) cameras: radiation with wavelength from  $8$  to  $14\mu m$

EO systems acquire knowledge of the target exploiting the photons emitted by the Sun and reflected from the TOI surface (VIS, NIR, and SWIR cameras), or exploiting the photons directly emitted by the target itself (LWIR cameras), or exploiting the combination of both the contributions (MWIR cameras). Infrared cameras allow the user to form an image using IR radiation, similar to common cameras that form an image using visible light. In particular, the radiation acquired from LWIR cameras is related to the temperature of the observed scene according to the Planck's law. In this framework, hyperspectral sensors sample the incoming radiation at many spectral bands, by means of a prism, or with interferometric technologies. Each spatial pixel forms a vector of measurements from different spectral bands. This vector, identified as the observed spectral signature, contains information about the materials present in the scene and can be exploited for detection, recognition, and identification [20]. The measure is a superposition of some spectral signatures coming from the background and the atmospheric layer, which separates the target in the scene from the sensor [20].

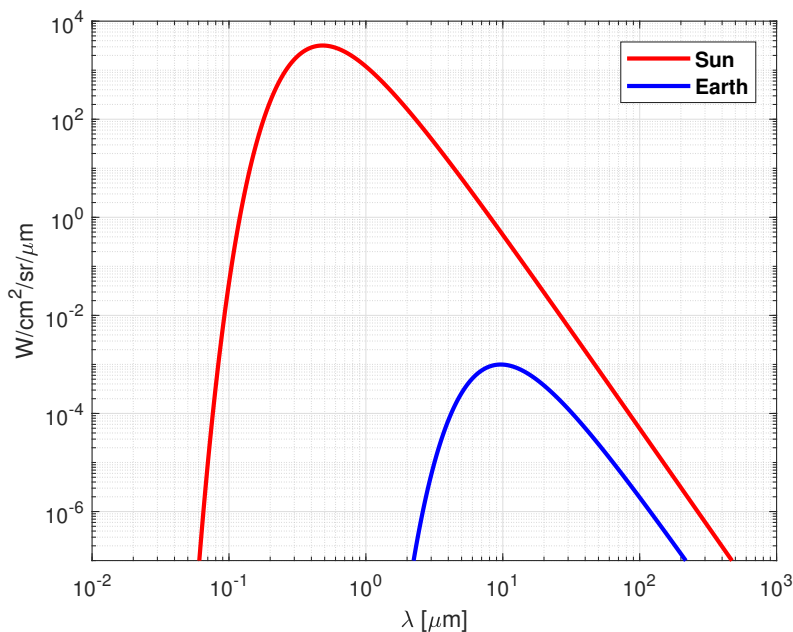


**Figure 1.1:** Comparison between Sun and Earth electromagnetic radiations represented as blackbodies at  $6000K$  and  $300K$ , respectively

As said previously, the Sun is the dominant radiation source in the VIS, NIR, and SWIR regions, while thermal emission of the targets dominate in the LWIR region.

## 1.2. Representation of Hyperspectral Images

The two sources of energy are roughly comparable in the MWIR; hence, both must be considered for sensors operating in this spectral region. LWIR is characterised by the thermal emission of objects and elements in the scene having a temperature different from 0K [16]. In the thermal infrared the ground thermal radiance presents a spectral peak around  $10\mu m$ , for a typical ground temperature between 230 and 370 K. The atmosphere absorbs and emits radiation in this spectral region. The atmospheric radiation is strictly dependent on its temperature and on water vapour concentration [12, 20, 21]. In Fig. 1.1, the Sun with the Earth radiation are considered as two blackbodies at 6000K and 300K, respectively. The scale of the y- and x-axes are logarithmic to achieve a better visualization of the phenomenon. The solar contribute is predominant with respect to the Earth one in the spectral region until  $2.5\mu m$ . Then, in the spectral range between 3 and  $6\mu m$ , the two spectral contributes can be exploited at the same time for remote sensing purposes. In the long wave infrared domain extending from 8 to  $14\mu m$ , the electromagnetic radiation source associated to the Earth can be maximally exploited, especially for night remote sensing missions. Thus, LWIR hyperspectral sensors catch the electromagnetic radiation produced by surfaces that experience typical earthly temperatures, i.e. between 230K and 370K.

## 1.2 Representation of Hyperspectral Images

Hyperspectral sensors perform simultaneous acquisitions of several information, from visible to far infrared depending on the deployed technology, which corresponds to several hundred images associated with different spectral bands for the same scene. By the nature of the hyperspectral data, in which each pixel is well represented by a vector, the data are typically represented by a hyperspectral cube. Because of this cubic representation of the data, it is natural to consider the use of *tensors* of the third order as a mathematical model for the analysis of hyperspectral images. Typically, the spatial variabilities are associated to the first and second dimensions of the tensor, respectively. The spectral variability of the pixels is associated to the third dimension of the tensor.

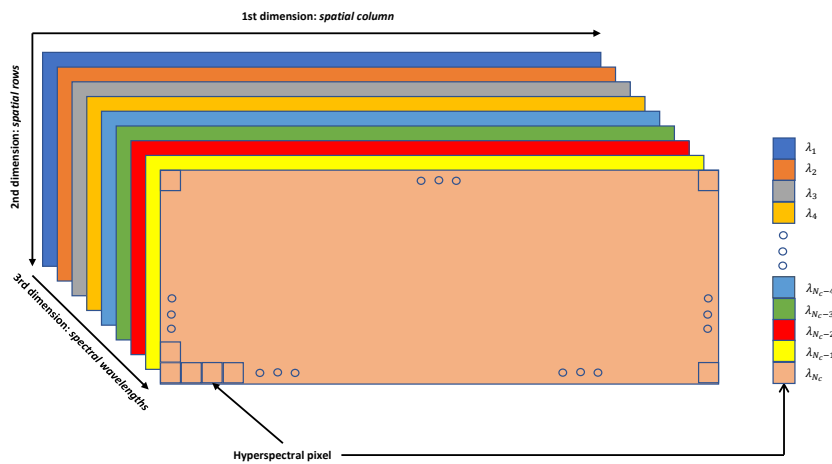


Figure 1.2: Illustration of the tensor representation of a hyperspectral image

Figure 1.2 depicts the tensor representation of a hyperspectral image. The different colors are visually associated with different spectral bands (the wavelength is identified with  $\lambda$ , and the maximum number of spectral channel of a sensor is identified as  $N_c$ ). The small squares within each layer is visually associated with a different spatial pixel of the Focal Plane Array (FPA).

Current-generation systems are divided in two main infrared spectroscopy technologies: *dispersive* systems and *FTIR* (Fourier-Transform IR) systems. The first systems employ a dispersive element, such as a prism or grating, to separate the individual frequencies ("colours") of energy emitted and/or reflected from the source. The detector measures the amount of energy at each frequency which has passed through the dispersive element. Instead, the second systems exploit an optical device called interferometer in order to produce a signal, known as "interferogram", that has information about every frequency which comes from the source. In order to obtain the spectrum of the signal, the Fourier Transform technique is applied to the interferogram.

The two spectroscopy technologies are further characterized by the scanning technique, i.e. the method by means the hyperspectral cube is acquired by the system:

- *Spatial Scanning*: the FPA outputs a full slit spectrum, that represents the spectra of all the pixels along one of the spatial dimensions of the hypercube (first and third dimensions of Fig. 1.2). In order to acquired a full hyperspectral image of the scenario, spatial scanning requires a per-lines analysis by means of a "pushbroom scanner". With this per-line system, the second spatial dimension is collected through the movement of a platform (airplane, drone, satellite and so on). The pushbroom scanners, also sometimes referred to as along-track scanners, use a line of detectors arranged perpendicular to the flight direction of the platform. As the platform flies forward, the image is collected one line at a time, with all of the pixels in a line being measured simultaneously. The slit image is focused and spectrally dispersed into several spectral components that are independently sensed.
- *Spectral Scanning*: the FPA outputs a monochromatic spatial image of the scenario, i.e. a bidimensional image captured at a fixed wavelength. In order to produce a full hyperspectral cube, the scanning technology requires optical band-pass filters, either tunable or fixed (for example interferometric systems). Thus, the scene is scanned by continuously switching the filters while the device remains stationary (observing the same scene). The advantage of such a system is that a scene is simultaneously captured, having a direct representation of its two spatial dimensions. In order to scan the entire area of interest, the system requires to be moved step-by-step and spectrally scan each scene portion.

### 1.3 Signal Model

---

In the LWIR domain, with  $\mathbf{L}_{as}$  is denoted the  $N_c \times 1$  vector whose components are the spectral samples of the at-sensor radiance taken at the central wavelengths  $\lambda_1, \dots, \lambda_{N_c}$  of the adopted sensor. The spectral radiance  $L_{as_k}$  at the output of the  $k^{th}$  spectral channel is obtained by weighting the pupil plane radiance with the spectral responsivity function  $SRF_k(\lambda)$  of the channel. Such filtering operation is performed as follows [20]:

$$\mathbf{L}_{as_k} = \frac{\int_{-\infty}^{+\infty} L_{as}(\lambda) SRF_k(\lambda) \delta\lambda}{\int_{-\infty}^{+\infty} SRF_k(\lambda) \delta\lambda} \quad (1.1)$$

where  $k = 1, \dots, N_c$ , and  $L_{as}(\lambda)$  is the incoming spectral radiance that reaches the hyperspectral sensor from the observed surface. The spectral responsivity function of a hyperspectral sensor is characterized by three parameters:

- the spectral band (generally spoken, a hyperspectral sensor may not exploit the entire spectral band for which it is developed);
- the spectral sampling frequency, i.e. how distant are the spectral channels between them within the exploited spectral band;
- the Full-Width at Half-Maximum (FWHM), i.e. the extent of the spectral responsivity function of the  $k^{th}$  channel, measured as the difference between the two extremes of the wavelength at which the responsivity is equal to half of its maximum value.

In the LWIR, the at-sensor radiance vector  $\mathbf{L}_{as}$  can be expressed by the following Radiative Transfer Model (RTM) [20]

$$\mathbf{L}_{as} = \mathbf{D}_\tau \mathbf{L}_{gl} + \mathbf{L}_\uparrow + \mathbf{N} \quad (1.2)$$

with:

- $\mathbf{D}_\tau$  is the  $N_c \times N_c$  diagonal matrix whose diagonal elements are the spectral samples of the atmospheric spectral transmittance  $\tau$
- $\mathbf{L}_\uparrow$  is the  $N_c \times 1$  upwelling atmospheric radiance vector (or path radiance)
- $\mathbf{L}_{gl}$  is the  $N_c \times 1$  ground-leaving radiance vector

$\mathbf{L}_{gl}$  in turn can be expressed as

$$\mathbf{L}_{gl} = \mathbf{D}_\epsilon \mathbf{L}_{BB}(T) + [\mathbf{I} - \mathbf{D}_\epsilon] \mathbf{L}_\downarrow + \mathbf{N}_1 \quad (1.3)$$

where:

- $\mathbf{D}_\epsilon$  represents the  $N_c \times N_c$  diagonal matrix whose diagonal entries are the samples of the target spectral emissivity  $\epsilon$
- $\mathbf{L}_{BB}(T)$  is the  $N_c \times 1$  vector of the spectral radiance of a blackbody at temperature  $T$  (Planck's Law, see Figure 1.1)
- $\mathbf{L}_\downarrow$  is the  $N_c \times 1$  vector of the spectral downwelling atmospheric radiance (or downward radiance)
- $\mathbf{I}$  is the  $N_c \times N_c$  identity matrix

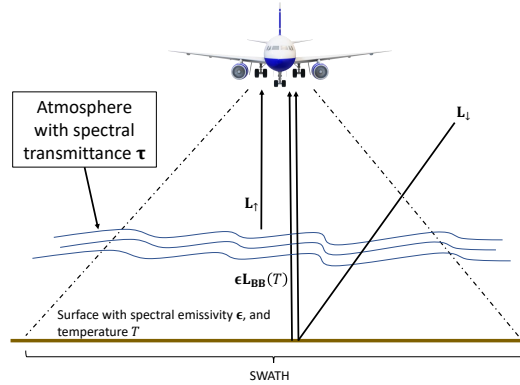


**Figure 1.3:** Graphical representation of the signal model for an airborne acquisition

With  $\mathbf{N}$  and  $\mathbf{N}_1$  are denoted the  $N_c \times 1$  noise vectors before and after atmospheric correction, respectively.

Fig. 1.3 shows the typical acquisition geometry of a remote sensing mission, performed by means of an airplane, where the hyperspectral sensor observes the scenario with a nadir view. The pushbroom scanning mode is implicitly assumed, hereinafter. Furthermore, the figure depicts the main radiation sources from the observed surface and atmosphere. During the dissertation, the pushbroom acquisition technology is implicitly assumed for all the considered hyperspectral sensors.

---

## Polynomial-fitting Temperature and Emissivity Separation

---

### 2.1 Introduction

---

Hyperspectral remote sensing in the Long Wave InfraRed (LWIR) provides useful information for geophysical and surveillance purposes. Objects with a temperature higher than absolute zero emit thermal radiations into the  $8\text{-}12\mu\text{m}$  region of the electromagnetic spectrum. Radiance measurements made in this spectral window allow surface spectral-emissivity and temperature estimation, which are thermal-optical intrinsic properties of the surface and its physical state. Furthermore, chemical identification of the objects can be performed without an external illumination source, allowing day/night operations [20]. The emissivity represents the spectral signature of a material that, equivalently to the spectral reflectance in the VIS/NIR/SWIR domains, allows identifying with certainty the object. If properly estimated, the emissivity allows the recognition and/or the detection of targets in the monitored scenario, exploiting the already-implemented algorithms and processing architectures for the domain of the reflected solar radiation [22]. Materials emissivity and temperature are tightly combined inside the measured radiance; their joint estimation represents a challenging task: assuming that the atmospheric effects have been completely compensated (see Eq. 1.2), the estimation is an ill-posed problem because, for the observed radiance at  $N_c$  sensor channels, there will always be  $N_c + 1$  unknowns, i.e. the temperature and the emissivity samples [12]. Besides, the atmospheric downwelling radiance and the surface-emitted radiance are also coupled together through the emissivity, making the estimation more complicated (see Eq. 1.3).

In the literature this problem is known as Temperature and Emissivity Separation (TES). During the last decades, many scientists have approached this underdetermined prob-

lem from different perspectives. In 1998, Gillespie *et al* [2] proposed a method that hybridizes three established algorithms, that starts estimating the normalized emissivities, and then calculating emissivity band ratios. Finally, it employs an empirical relationship to predict the minimum emissivity from the ratioed values spectral contrast, permitting emissivity spectrum recovery. In the same year, Borel proposed the Iterative Spectrally Smooth TES (ISSTES) method [6]. The algorithm considers the surface emissivity a smooth function of the wavelength, with respect to the atmospheric downward spectral radiance, which contains numerous gaseous emission lines. Emissivity spectra are first computed using a series of surface temperatures near the true surface temperature. Then, the emissivity spectra smoothness is iteratively computed, and the smoothest emissivity spectrum is selected as the best surface emissivity estimate. The corresponding temperature is used as the surface temperature estimate. In 2010, Cheng *et al* proposed the Stepwise Refining TES (SRTES) [13]. SRTES utilizes the atmospheric downward spectral radiance residue in the calculated surface self-emission as a criterion, and adopts a stepwise refining method to determine both the emissivity at the location of an atmospheric emission line in a narrow spectral region, and the surface temperature. In 2011, Wang *et al* proposed the Linear Emissivity Constraint TES (LECTES) [24]. LECTES is based on the problem of unknowns reduction, assuming that the emissivity spectrum can be described by a piecewise linear function. In 2017, Pivovarník *et al* proposed an optimized version of [2], denoted Optimized Smoothing TES (OSTES) [19]. The authors replace the first module, described in [2], with a new one, based on the spectral radiance signatures smoothness, and exploits an optimized approximation of the brightness temperature – emissivity relationship. In 2019, Acito *et al* proposed the Subspace-based TES (SBTES) [23]. They derive a general class of TES algorithms, relying on the assumption that the emissivity spectra of natural and man-made materials can be well represented in a given subspace of the original data space. The proposed approach originates several algorithms whose specific form depends on the particular basis matrix adopted to address the emissivity subspace. The different TES strategies have been derived starting from different assumptions, and using different approximations/simplifications, strictly related to the characteristics of the sensor, and to the materials spectrum searched in the monitored scene. The methods proposed in [2] and [19] cannot be applied to low emissivity materials (mean value of  $\epsilon \leq 0.6$ ), such as mostly metals. The ISSTES [6], and the SBTES [23] may provide low accuracy if the smoothness assumption is not verified. The SRTES [13] needs the knowledge of spectral regions where strong atmospheric emission lines are expected. The LECTES [24] can be set with different configurations, each one with different performance over different materials.

In this framework, a new algorithm called Polynomial-fitting TES (PTES) is presented. PTES is based on a mixed approach between [6] and [24]. The proposed algorithm is presented in two versions: in Sec. 2.2 the technique supposed that the atmospheric correction has been already carried out, i.e. the atmospheric terms of Eq. 1.2 are estimated by means of ancillary data (provided by an aerostatic balloon), or some automatic atmospheric correction techniques [8, 10, 21, 32]. The algorithm exploits an optimization procedure, estimating the best temperature that minimizes the atmospheric-residual features inside the emissivity spectral shape. The technique performs in a spectral interval, smaller with respect to the entire sensor spectral range, where the emissivity

is maximally smooth. Such interval is selected automatically by the algorithm, which quantifies the smoothness of the material signature as the standard deviation of the ground-leaving radiance derivative after an erosion-moving average filtering procedure. This operation allows one to mitigate the downward radiance contribution into the signal, and relate the smoothness directly to the self-emitted radiance, thus to the emissivity variability (being the Planck's law an extremely smooth function). Instead, in Sec. 2.3, the proposed algorithm is presented in a version, where a new atmospheric correction (AC) technique is joint to the previously shown TES algorithm. In the latter case, the indeterminateness is solved exploiting an optimization procedure, by estimating the best target temperature and atmospheric integrated water vapor (or total column water vapor, indicated as  $w$ ) that minimize the atmospheric-residual features inside the emissivity spectral shape. To perform the AC of the at-sensor radiance, a Look-Up-Table (LUT) of atmospheres is provided as input of the algorithm. The latter allows both to solve the TES problem, and to estimate the  $w$  content of the monitored scenario. In this chapter, the TES problem is simplified making the hypothesis that the atmosphere depends by only  $w$ . To make the problem easily treatable, standard information about  $\text{CO}_2$ ,  $\text{O}_3$ , aerosol and temperature profiles are used. The latter are commonly available within the MODTRAN environment [1]. The generalization of the problem to a more complex combination of atmospheric elements does not carry useful information to the TES technique that is proposed. In order to present the developed algorithm, the characteristics of a sensor operating in the  $8\text{-}12\mu\text{m}$  spectral range is assumed, featuring  $N_c = 133$  spectral channels corresponding to a Full-Width at Half-Maximum (FWHM) of around 30nm.

## 2.2 PTES algorithm

As already pointed out, if an erroneous temperature estimate is used to retrieve the emissivity from 1.3, atmospheric emission/absorption lines appear on the signature spectral shape [6]. As shown in Fig. 2.1, the sharp oscillations appear because the atmosphere is not completely compensated on the signal. The actual ground-leaving radiance was obtained using a temperature of 300 K, and a brick spectrum taken from the Urban Micromet spectral library [30].  $L_{\downarrow}$  was generated with MODTRAN [1] using a standard Mid-Latitude Summer atmosphere. As depicted, an underestimation of the temperature leads to an emissivity higher than 1, i.e. physically meaningless. Instead, an overestimation of the temperature provides a lower spectral signature, that still contains sharp atmospheric features.

The proposed PTES algorithm follows the strategy of unknowns-reduction and smoothness evaluation used in previous approaches ([6], [24]), but differs from them by the subsequent points:

- LECTES and ISSTES perform the TES task on the entire sensor spectral response. PTES defines a smaller spectral band, composed of a set of samples selected in the smoothest portion of the emissivity.
- Instead of a linear regression, as in [24], and a box-car filtering as in [6], PTES performs a  $N_{poly}^{th} > 1^{st}$  degree polynomial-fitting in the selected spectral portion. The higher degree, with respect to LECTES, allows to fit with a smaller error the shape of the emissivity, and to preserve the features. Furthermore, fitting

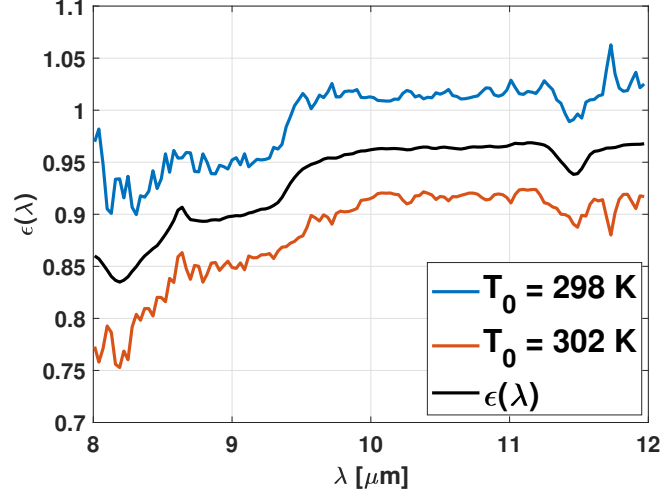


**Figure 2.1:** Effect of an erroneous temperature estimate on the emissivity retrieval (signal model inversion of Eq. 1.3)

the emissivity in a narrow interval, allows to avoid catching region where the smoothness constraint falls.

- The unique variable is the object temperature. The fitting quality is measured by the mean square error (mse) between the estimated emissivity for the selected temperature, and its  $N_{poly}^{th}$ -order polynomial-fitting. The mse is minimum when the estimated temperature is close to the actual one, i.e. the atmospheric residual features are minimized inside the emissivity spectral shape.

The algorithm is easily described by the following minimization problem:

$$\hat{T} = \arg \min_{\beta \in [T_L, T_H]} \frac{1}{N_c} \sum_{N_c} \left[ \frac{\hat{\epsilon}_T(\beta) - \hat{\epsilon}_{fit}(\beta)}{\hat{\epsilon}_{fit}(\beta)} \right]^2 \quad (2.1)$$

where  $\hat{\epsilon}_T$  is the estimate of the surface spectral emissivity, obtained by inverting the signal model in Eq. 1.3 within a spectral interval  $\Delta$  smaller than  $[8 - 12] \mu m$ , and given an attempt value of the surface temperature  $\beta$

$$\hat{\epsilon}_T = \frac{\mathbf{L}_{gl}(\Delta) - \mathbf{L}_{\downarrow}(\Delta)}{\mathbf{L}_{BB}(\Delta, \beta) - \mathbf{L}_{\downarrow}(\Delta)} \quad (2.2)$$

Instead,  $\hat{\epsilon}_{fit}$  represents the polynomial-fitting, in a least-square sense, of  $\hat{\epsilon}_T$  with degree  $N_{poly}^{th}$ , still within the spectral interval  $\Delta$ .

The minimization in Eq. 2.1 is performed by varying  $\beta$  between a minimum ( $T_L$ ) and a maximum ( $T_H$ ) temperature, set on the basis of the characteristics of the observed scenario. Once the temperature is estimated, the emissivity can be extracted from Eq. 1.3. In the subsequent experimental analysis,  $N_{poly} = 3$  has been chosen. Challenging task is the selection of the spectral interval  $\Delta$ , in which to apply the technique, that would require the knowledge of the monitored material. Since a 3<sup>rd</sup> degree polynomial-fitting is applied, the material signature should be sufficiently smooth. Basically, the polynomial degree could be increased, but leading to a higher computational cost, and

introducing errors provided by the fitting of atmospheric "impurities" and/or noise on  $L_{gl}$ . One possible solution is to perform the algorithm in several spectral regions, and select the one that reaches the lowest mse of Eq. 2.1. Another option is to reduce the effect of the downward radiance in Eq. 1.3, by means of an *erosion-moving average filtering* procedure, as explained in the following section.

### 2.2.1 Spectral Interval Selection

The term *erosion* is used to refer to a morphological operation that applies a moving window of size  $M$  to detect local minima of the input signal. Basically, the erosion filter is a sliding min-filter that outputs a step-signal, where each sample represents the minimum value of the input signal inside the moving window. Fig. 2.2b shows the erosion procedure on a ground-leaving radiance obtained using the aluminum-zinc sample of the library [30] (Fig. 2.2a). The atmosphere and temperature are the same as in Fig. 2.1.

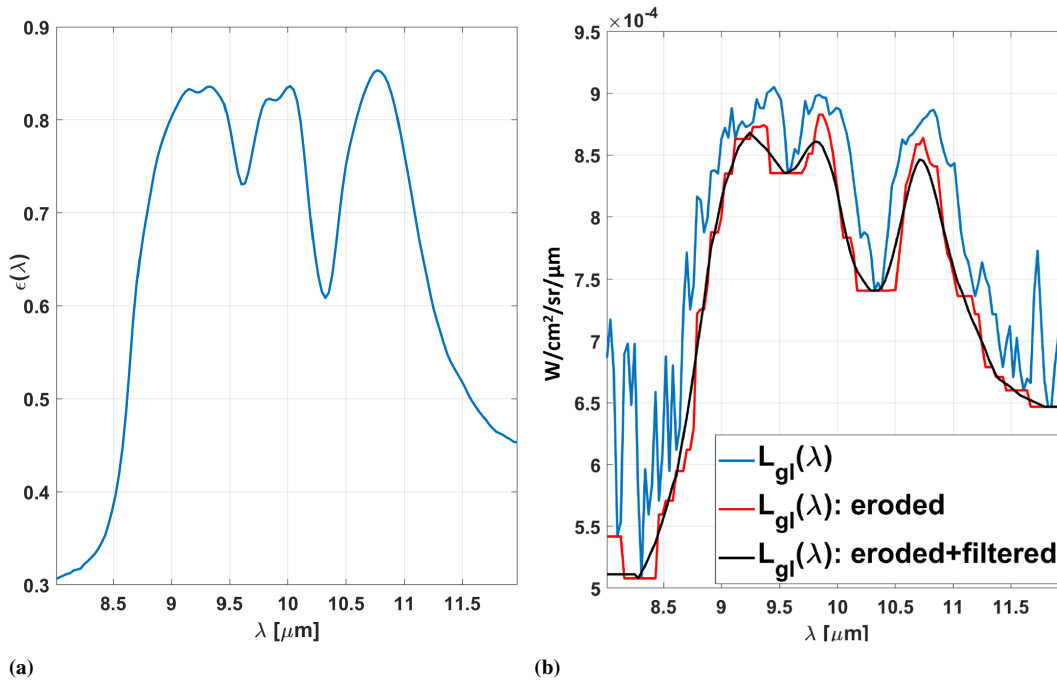


**Figure 2.2:** Effects of the erosion-filtering procedure. (a) aluminum-zinc spectral emissivity. (b)  $L_{gl}$  and its eroded (red) and eroded-filtered (black) versions

As shown, the eroded signal follows the lower envelope of the ground-leaving radiance, attenuating the effect of the downwelling radiance, but providing a step version of it (red curve), that may corrupt the successive smoothness measurements. In order to avoid the problem, a moving average filter is applied on the eroded  $L_{gl}$ . As depicted in Fig. 2.2b, the eroded-filtered signal (black curve) follows the shape of the emissivity. This means that they share also equivalent derivatives (except for an irrelevant scaling factor). Measuring the standard deviation of the derivative of the eroded-filtered  $L_{gl}$  in different spectral intervals, the algorithm automatically decides, in a blind manner, for the smoothest region  $\Delta$  where the PTES algorithm has to be applied, i.e. the one with

the lowest standard deviation. In Fig. 2.2b,  $M = 10$  has been used for both the moving window of the erosion and average filters.  $M$  must consider the sensor spectral resolution, and the features of  $L_{\downarrow}$ . In this case, it has been chosen evaluating the compromise between the computational complexity of the algorithm, and the reconstruction error between the eroded-filtered emissivities, and their original versions, for the available dataset in [30]. For  $M = 10$ , the mse is always well under -20 dB.

In order to apply the proposed method, the LWIR spectral range has been divided in four bands:  $[8 - 9] \mu m$ ,  $[9 - 10] \mu m$ ,  $[10 - 11] \mu m$ , and  $[11 - 12] \mu m$ . The choice is entirely arbitrary. To avoid this constraint, one can use a sliding window that dynamically assesses the smoothest spectral interval, without splitting the entire sensor spectral range. Of course, such a solution is computationally more expensive. Easier solution is to increase the number of sub-bands, reducing the number of samples for each interval, and eventually partially overlap them.

### 2.2.2 Experimental Results

In order to assess the performance of the proposed method, four different emissivity spectra have been selected from the Urban Micromet spectral library [30]. The database contains 82 spectral signatures, related to materials commonly found in a typical urban environment. The selected spectra of Fig. 2.3 have been chosen to analyze high, low, and high spectral dynamics emissivity materials.

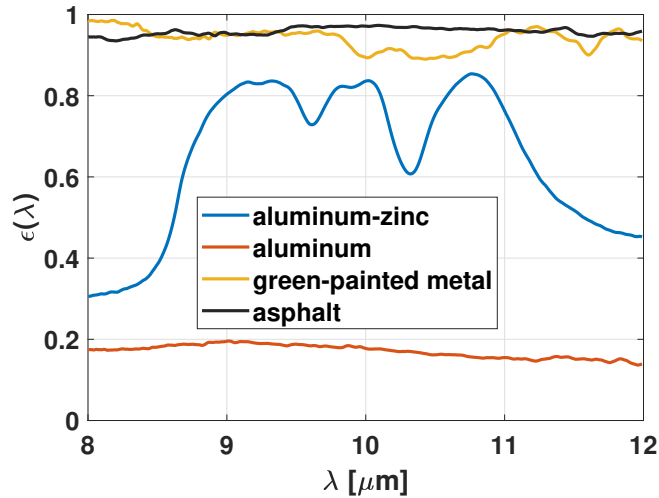


**Figure 2.3:** Spectral signatures used for the simulations

All the experiments have been carried out by means of MODTRAN [1], to simulate realistic values of  $L_{gl}$  for a standard Mid-Latitude Summer atmospheric condition and a given object emissivity. The assumed temperature is 300K. Figure 2.4 and 2.5 show the results for the high spectral emissivity materials. For the asphalt sample, the selected spectral interval is  $\Delta = [10 - 11] \mu m$ ; instead, for the green-painted metal, the selected portion of the spectrum is  $\Delta = [8 - 9] \mu m$ . In both cases, the smoothness of the signatures in those intervals are clearly visible. The estimated temperatures have errors lower than 0.3K and 0.1K, respectively. For the metal sample, the estimated emissivity and the actual one are not discernable, highlighting the satisfactory performance of PTES respect to the common remote sensing application requirements [18].

Fig. 2.6 shows the result for the aluminum-zinc material, that presents an emissivity featuring high spectral dynamics and a mean value of 0.65. The selected spectral band is  $\Delta = [11 - 12] \mu m$  which is well approximated with a 3<sup>rd</sup> degree polynomial. The temperature estimate reaches an accuracy of less than 0.4K, thus satisfactory for mostly applications [18]. Fig. 2.7 shows the results for the aluminum sample, i.e. extremely low emissivity material. Since the ground-leaving radiance is mostly composed by the downward radiance, many TES algorithms fail on this type of material [2, 12, 18, 19]. The challenging task is represented by the temperature estimation. In this case, PTES yields high accuracy, with a temperature error less than 2K. The selected spectral interval  $\Delta = [10 - 11] \mu m$ . Notice that, even though the performance are worse than with the previous materials, low emissivity objects are less commonly encountered than high emissivity ones. For example, the library in [30] contains only one low emissivity spectrum (aluminum), on an amount of 82 spectra. Furthermore, as shown in [30], if the aluminum is exposed to weather, its emissivity increases, becoming a high emissivity object, leading to performance comparable with the ones previously shown.

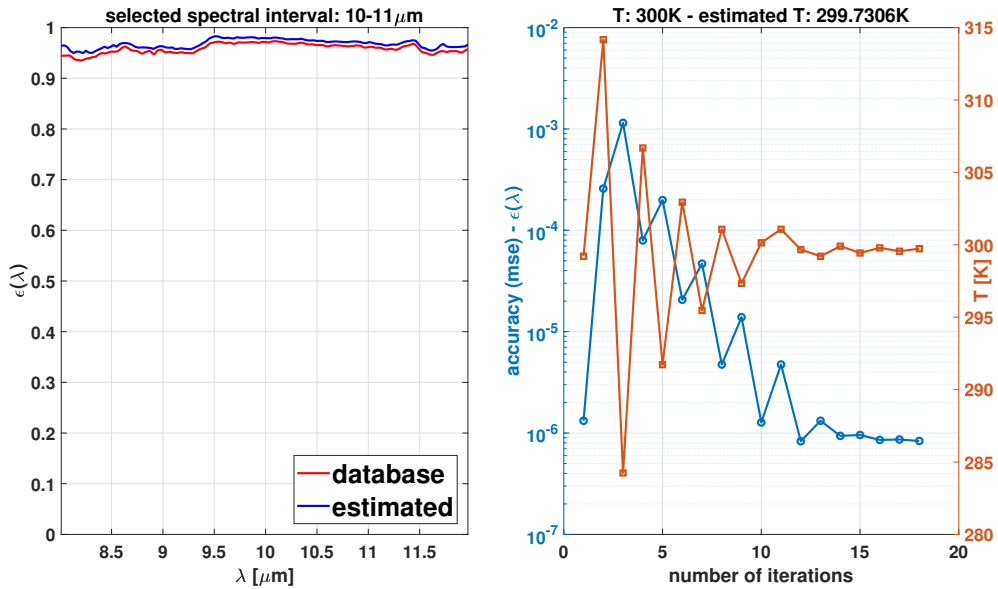


Figure 2.4: Result for asphalt sample

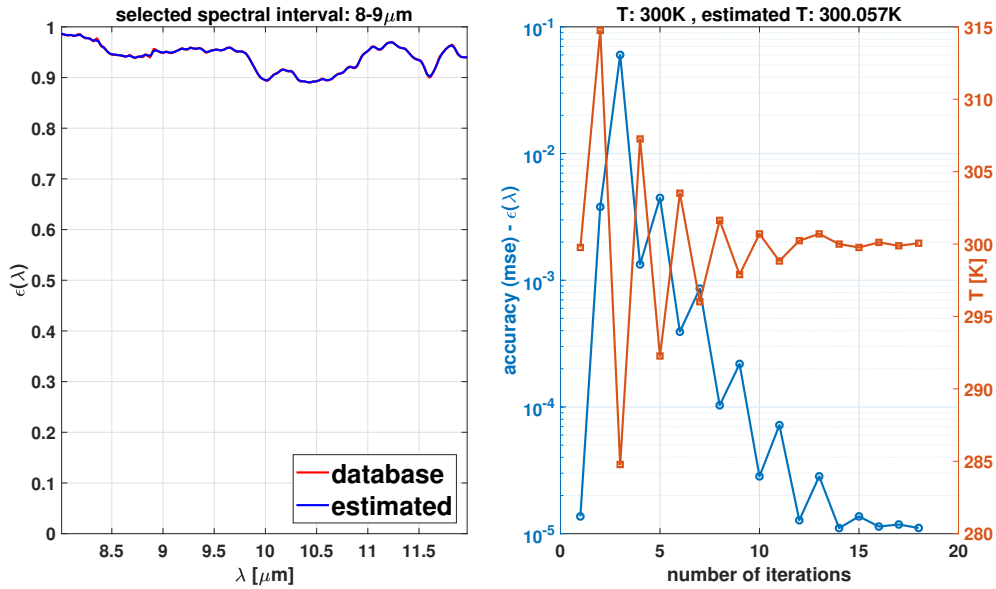


Figure 2.5: Result for green-painted metal

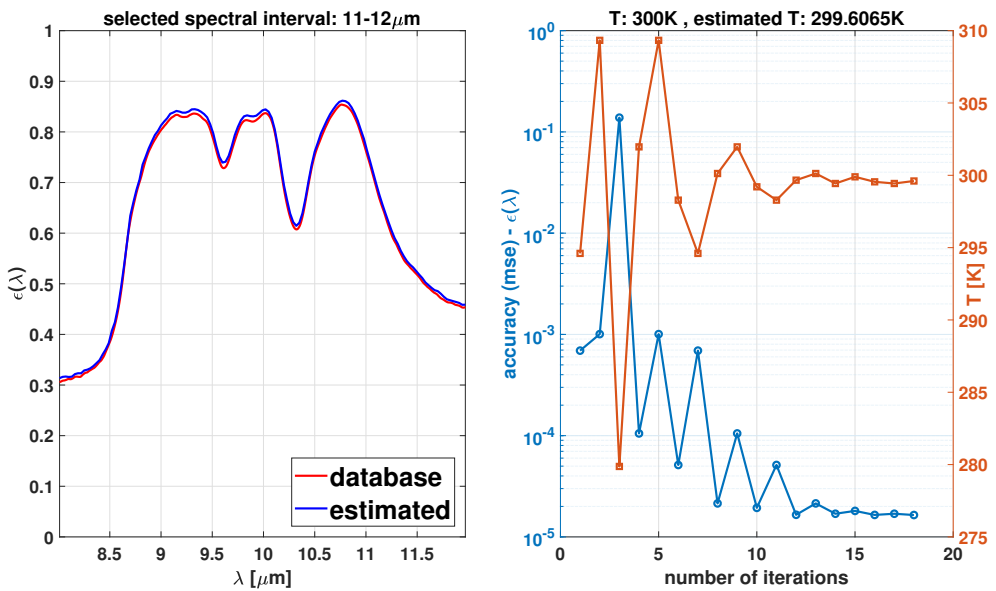


Figure 2.6: Result for aluminum-zinc sample

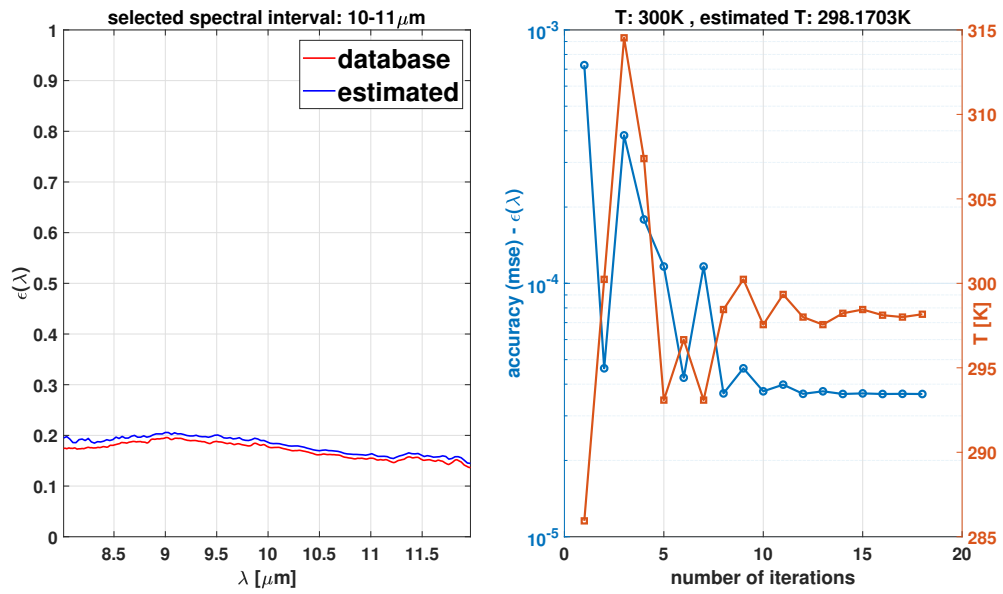
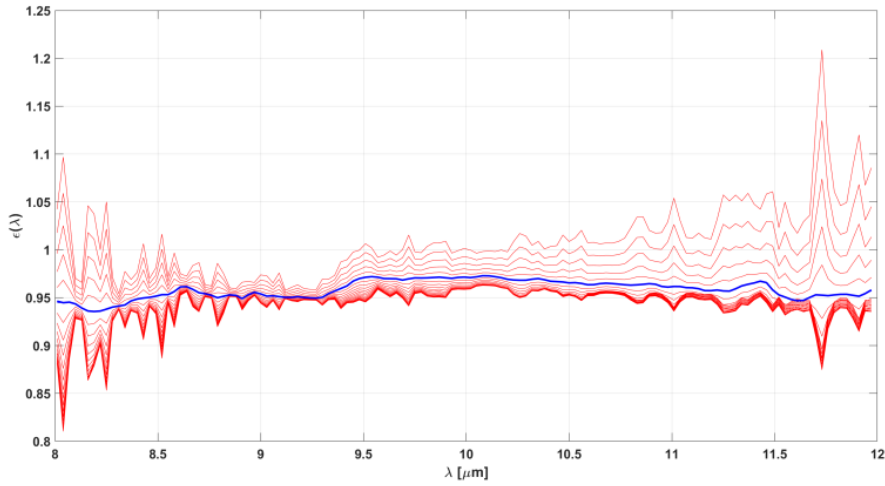


Figure 2.7: Result for aluminum sample

### 2.3 PTES with Atmospheric Correction

As it has been already pointed out in Sec. 2.2, if an erroneous estimate of  $T$  is used to retrieve the emissivity from Eq. 1.3, atmospheric emission lines appear on the signature spectral shape (Fig. 2.1). Of course, the same effect is obtain if a not proper estimates of the atmospheric elements (see Eq. 1.2) are provided to the algorithm. Fig. 2.8 shows an example of the effects (red curves), starting from the at-sensor radiance of an asphalt sample [30], for different error combinations of  $T$  and  $w$  (actual value:  $T = 300\text{K}$ ,  $w = 2\text{gr}/\text{cm}^2$ ). The blue curve is the true spectral emissivity. The sharp oscillations clearly identify the atmospheric residuals, let also the emissivity be greater than one, i.e. meaningless. The flattest solution is obtained only if  $T$  and  $w$  assume the exact values by which the radiance is simulated.



**Figure 2.8:** Effects of a wrong estimate of  $T$  and  $w$

In this framework, the PTES algorithm featuring the atmospheric correction is easily described by exploiting the already presented Eq. 2.1 and 2.2, expanding the dissertation to consider  $w$  as new unknown, in addition to  $T$ . As in Sec. 2.2, the best pair  $(\hat{T}, \hat{w})$  is found by minimizing the mean square error (mse) between the estimated emissivity, and its  $N_{poly}^{th}$ -order polynomial fitting within a given spectral interval. The function assumes the lowest value when the residual atmospheric emission lines are minimized along the emissivity shape. In order to obtain the optimal  $w$  that allows to perform the atmospheric correction, the algorithm exploits a LUT of atmospheres, in terms of  $L_{\downarrow}$ ,  $L_{\uparrow}$ , and  $\tau$ , parameterized with respect to  $w$  itself, commonly unknown in operative scenarios. Since many parameters are known during a remote sensing mission, such as the day of the year, time of the day, acquisition geometry (flight quota and viewing angle), and atmosphere model [1, 12], the LUT is obtained by running several times MODTRAN, by fixing those parameters and by tuning the  $w$  value. Performing an interpolation along all the wavelengths in the chosen window, the algorithm is automatically able to estimate the water vapour that best explains, jointly with  $T$ , the measured at-sensor radiance. At the end of the optimization procedure, the problem is no more underdetermined, and an estimate of  $\epsilon$  is obtained.

Parameter	Value
Atmosphere model	Mid-Latitude Summer
Flight quota a.s.l.	1 Km
Target quota a.s.l.	0 Km
Viewing angle	180° (Nadir-view)
Day of the year	July 19 <sup>th</sup>
Time of the day	12:00
Latitude-Longitude	43.46°N-11.2°E (Florence)
$w$	0.5 gr/cm <sup>2</sup>
Target temperature	300K

**Table 2.1:** Parameters used for the atmosphere simulation

### 2.3.1 Analysis of the spectral window

In order to perform the TES task, a spectral window must be provided, in which the proposed solution is applied. As already pointed out, it has to be composed of a set of samples, where the emissivities are particularly smooth. In this example,  $N_{poly}^{th} = 3$  has been chosen to best approximate the emissivity curve in the selected portion.

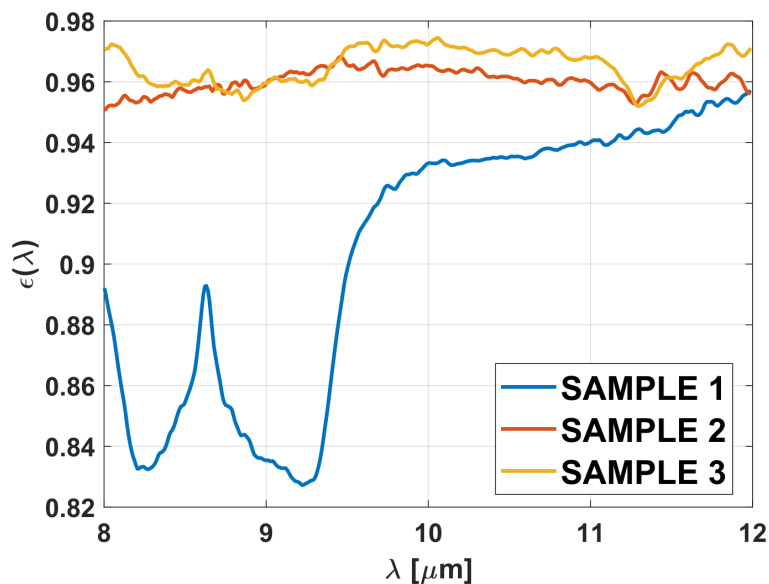


**Figure 2.9:** Spectral emissivities of the class "quartzite"

Several analyses have been carried out with the class quartzite of the library in [30], shown in Fig. 2.9. This class is particularly suitable for the purposes, because it contains materials with both low and high spectral dynamics. In order to identify the best spectral window, the at-sensor radiances for the three emissivities have been simulated, starting from the parameters in Table 2.1, supposing an airborne remote sensing mission.

By exploiting the LUT generated with  $w$  values spread in 0.1 – 5 gr/cm<sup>2</sup>, the three at-sensor radiances are atmospherically compensated, and emissivities are retrieved by using the true target temperature (Table 2.1). Once the spectral signatures are estimated, a minimum value of the rmse between the estimated emissivity and the actual emissivity

was expected, for the water vapour value by means the atmosphere has been generated. By carrying out several analysis and investigating the procedure for different  $w$  values, the results suggested that the most suitable spectral window is  $8 - 9\mu\text{m}$ . Figure 4 shows an example of the obtained rmse curves for  $w = 0.5\text{gr}/\text{cm}^2$ .

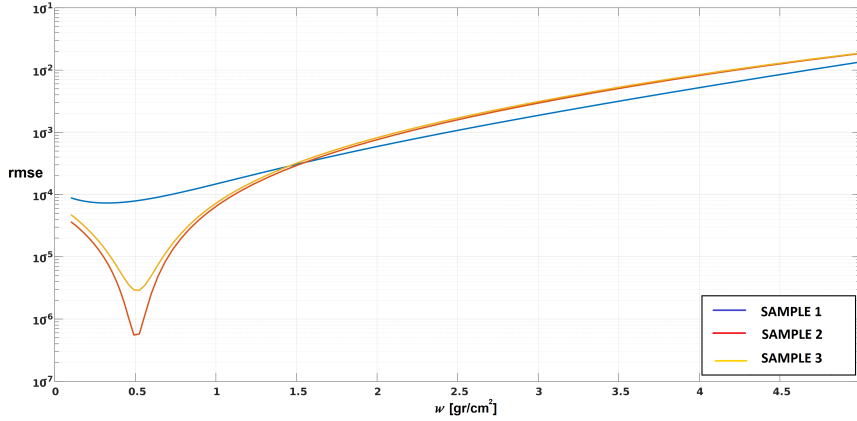


**Figure 2.10:** *rmse between the actual spectral emissivity, and the one obtained by means of the PTES algorithm, in the case that the algorithm is applied within the  $8-9\mu\text{m}$  spectral band, for a standard atmosphere with a water vapor concentration of  $0.5\text{gr}/\text{cm}^2$ . The minimum value of the rmse is obtained when the atmospheric correction is performed exploiting the entry of the LUT at the actual water vapor concentration*

As expected, the rmse has a deep minimum value for samples 2 and 3, that are actually smooth in  $8 - 9\mu\text{m}$ . Instead, sample 1 presents a sharp feature around  $8.5\mu\text{m}$  (Fig. 2.9) and its related rmse curve presents a flat behaviour at  $0.5\text{gr}/\text{cm}^2$ . Noting that in this window there are small spectral portions where the emissivities are simultaneously smooth, new experiments have been carried out by restricting the analysed spectral window. Results have suggested that the most suitable interval is  $8 - 8.3\mu\text{m}$ . Fig. 2.11 shows the benefits of the smaller window.

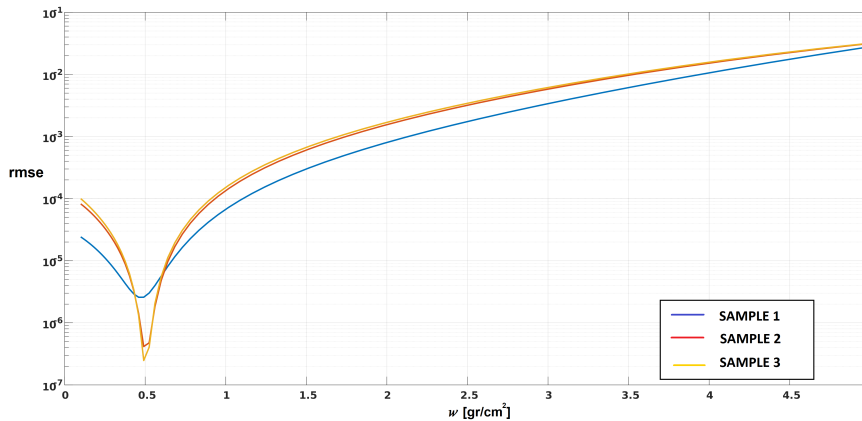


**Figure 2.11:** *The figure presents the same result of Fig. 2.10, but performing the algorithm in a smaller spectral interval:  $8-8.3\mu\text{m}$*

In this window the rmse assumes its lowest value, with a sharp and deep minimum value at the actual  $w$  content, regardless the material and temperature. Experiments

have been carried out also for concentrations of 1, 2, 2.5, and  $3\text{ gr/cm}^2$ , achieving the same results. For the supposed hyperspectral sensor, this interval contains 11 samples. As it is shown in Fig. 2.9, in  $8 - 8.3\mu\text{m}$  the emissivities are simultaneously extremely smooth. In order to clarify,  $w$  values have been chosen according to the average water vapour content of the Earth's mid-latitude area, European region [25].

### 2.3.2 Experimental results

In order to validate the proposed technique, both in terms of TES task and estimation of the integrated water vapour content of the atmosphere, PTES has been deployed to retrieve, from simulated at-sensor radiances, the materials emissivities shown in Fig. 2.12. The depicted materials have been chosen in order to cover all the possible features of a given spectral emissivity, namely: high value, low value, and high spectral dynamics.

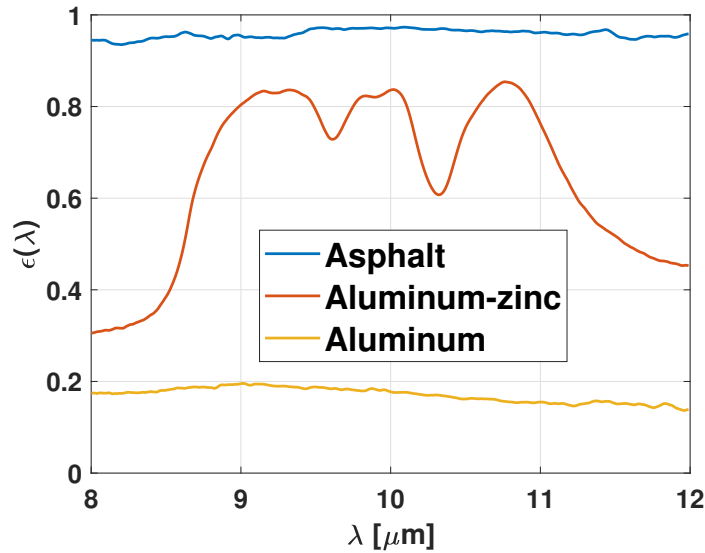


**Figure 2.12:** Spectral emissivities of the selected materials chosen for the experiments

At-sensor radiances have been generated for several combinations of  $w$  concentrations between  $1 - 3\text{ gr/cm}^2$  and temperatures between 270-330K [25], both for summer and winter atmospheres. The two atmospheres define different aerosol type and concentrations [1]. This large combination of parameters allows determining potential and limitations of the proposal. The remaining atmospheric parameters, that define and complete the scenario, are the ones of 2.1, except for the already aforementioned ones. In case of wintry atmosphere, the day is January 20<sup>th</sup>.

In order to evaluate the performance of PTES with the atmospheric correction, three merit figures are defined. The first two are the absolute values of the differences between the actual value of  $T$  and  $w$ , and their estimates obtained by means of the algorithm, respectively. They are denoted as  $\text{bias}_w$  and  $\text{bias}_T$ . Instead, the third merit figure is the root mean square error between the actual spectral emissivity and its estimate from PTES, weighted by the actual emissivity:

$$\text{RMSE}_\epsilon = \sqrt{\frac{1}{N_c} \sum_{i=1}^{N_c} \left[ \frac{\epsilon_i - \hat{\epsilon}_i}{\epsilon_i} \right]^2} \quad (2.3)$$

where the subscript  $i$  indicates the dependency of the emissivity from the wavelength.

The experiment does not pretend to define the performance of the PTES algorithm with absolute strictness. Its results have to be considered in the framework of a general evaluation for its deployment in a real context, where commonly  $w$  and  $T$  are unknowns. These simulations are expected to identify a feasibility trend for each material, in terms of object temperature and atmospheric features. Namely, a region in such "space" where the spectral emissivity is well reconstructed, and the temperature and the integrated water vapor values are well estimated from the at-sensor radiances. Concerning the LUT, parameterized with respect to the water vapor concentrations, tests have shown that six values, equal to 0.1, 1, 2, 3, 4, and 5  $gr/cm^2$ , are enough to reconstruct any atmosphere, at a  $w$  value between the aforementioned ones. The rmse, obtained between the reconstructed atmosphere and the actual one from MODTRAN, is always smaller than -30dB.

#### Results for high emissivity

Fig. 2.13 (a)-(d) show the results obtained for the asphalt sample. The *hot* maps (left column), represent the results for summer atmosphere; instead, the *cold* maps (right column) represent the results for wintry atmosphere.

#### Results for high spectral dynamics emissivity

Fig. 2.14 (a)-(d) show the results obtained for the aluminum-zinc sample. The *hot* maps (left column), represent the results for the summer atmosphere; instead, the *cold* maps (right column) represent the results for the wintry atmosphere.

#### Results for low emissivity

Fig. 2.15 (a)-(d) show the results obtained for the aluminum sample. The *hot* maps (left column), represent the results for the summer atmosphere; instead, the *cold* maps (right column) represent the results for the winter atmosphere.

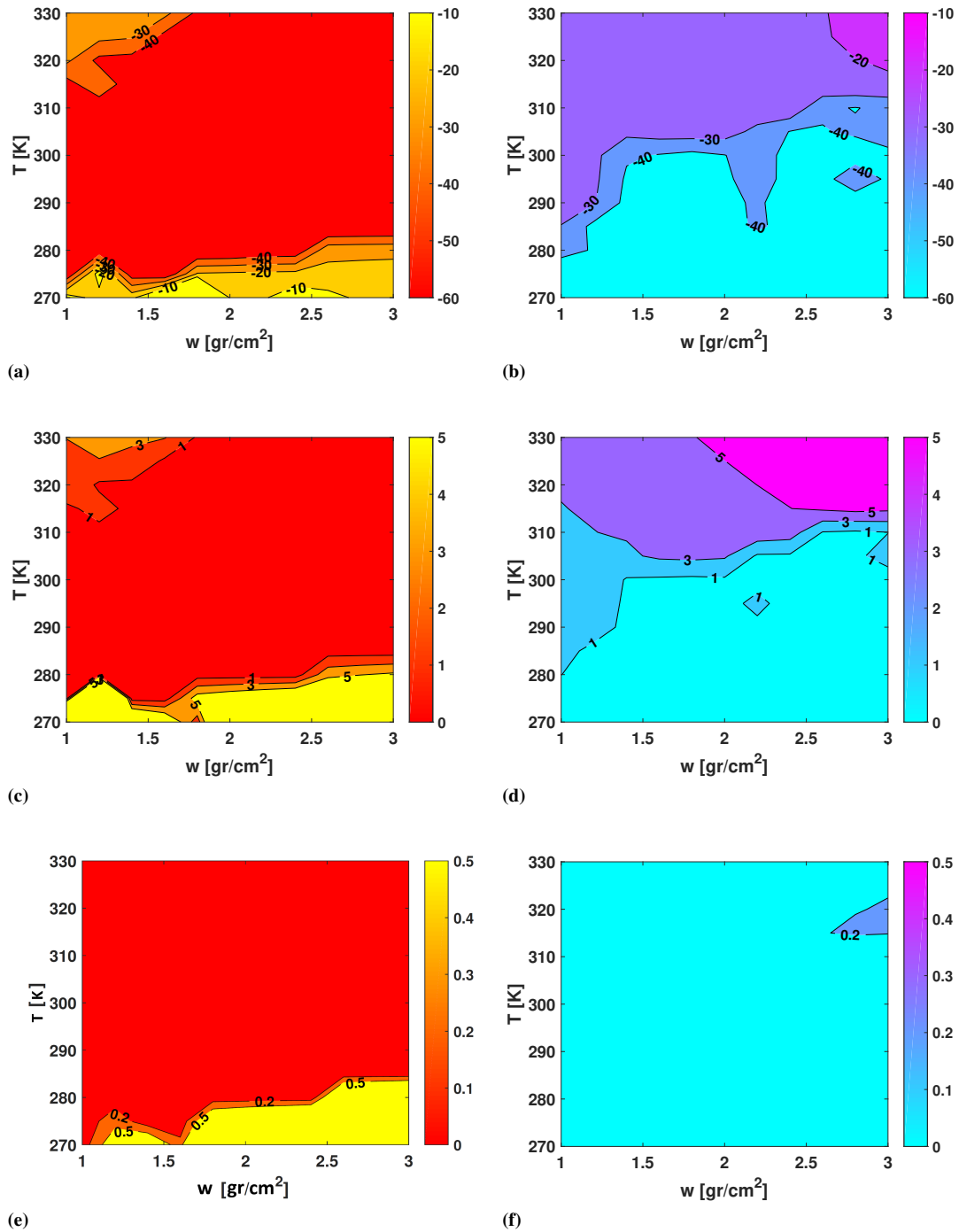
### 2.3.3 Discussion

The previous results show that, generally, the performance goes varies with respect to the analysed spectral signature. Fig. 2.13 (a)-(d) present a rmse that is always lower than -20dB, which is consistent with the requirements of most of applications [18], and temperature and integrated water vapor bias that are lower than 3K and 0.2 $gr/cm^2$ , respectively. The results for the summer and wintry atmosphere seem to feature symmetric behaviour. The degradation happens at really low temperature for the summer case, namely when the atmosphere is much warmer than the target temperature [24]. However, during summer it is quite unlikely to find a cryogenic-cooled target and, eventually, on its surface it would be present ice or moisture that corrupt the emissivity measurement. For the wintry atmosphere, degradations occur in case of high object

temperature and high atmospheric integrated water vapour, where a complex interaction between the surface-emitted radiance and the up/downwelling radiances may lead to a bad execution of PTES. However, it is unlikely to experience  $w$  beyond  $2gr/cm^2$  during winter [25].

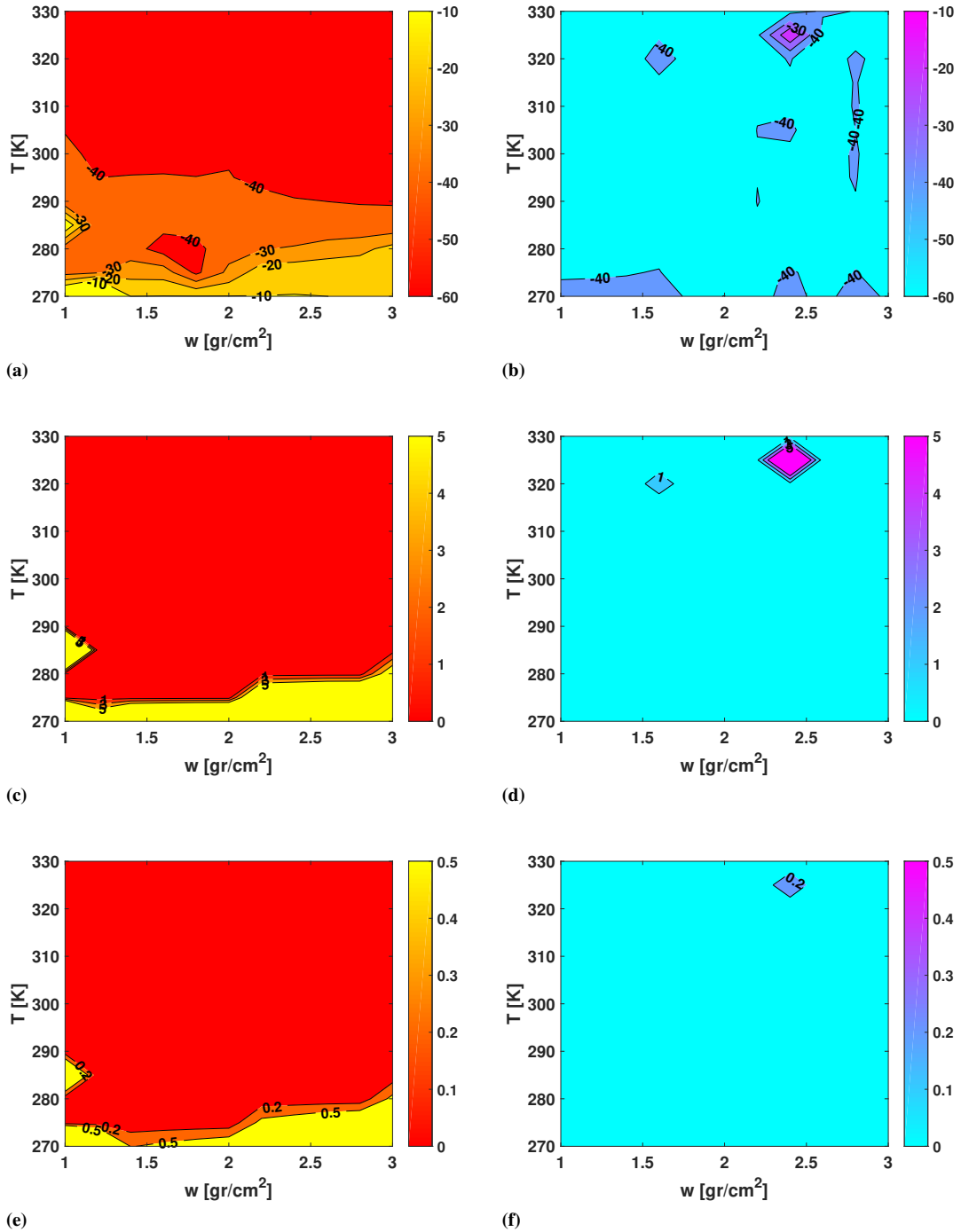
Fig. 2.14 presents the results for the aluminum-zinc sample, namely the high spectral dynamic target. The maps show the high performance achieved, that may be linked to the higher information carried by this type of material, with respect to flat emissivities. For the summer atmosphere, conclusions about degradation are the same as for the asphalt sample previously described. Instead, for the winter and dryer atmosphere [24], the PTES reaches its best results, being the environment less prone to corruptions of the self-emitted radiance from the object.

Fig. 2.15 shows the results for the low-emissivity aluminum sample. In the case of summer atmosphere, positive trend is recorded for  $T$  between 280-320K and for  $w$  between  $1.5-3gr/cm^2$ . Outside this region, the performance goes degrading quickly. For low temperatures, similar conclusions can be inferred as for the asphalt and aluminum-zinc samples; furthermore, the low spectral emissivity leads to an even lower radiative transfer from the target, thus a complete concealment of the self-emitted radiance carried out by the atmospheric radiances. Perceptible degradations are recorded also for high target temperatures, because the coarse temperature estimate affects the estimation of the spectral signature (over-estimation). The degradation can be eventually reduced during the subsequent detection step, by subtracting the mean values from the estimated emissivity, and the one from the database [31]. In case of winter atmosphere, degradations occur only for temperatures higher than 300K, because of a coarse temperature estimate of the object. Notice that, even though the performance are worse than with high emissivity materials, low emissivity objects are less commonly encountered than the high emissivity ones. For example, the library in [30] contains only one low emissivity spectrum (i.e. aluminum), out of 82 spectra. Furthermore, as shown in [30], if the aluminum is exposed to weather, its emissivity increases, becoming a high emissivity object, which leads to performance that are comparable with the ones of the other investigated materials.



**Figure 2.13:** Asphalt sample. (a) and (b) represent the  $rmse_{\epsilon}$ , expressed in dB, between the actual spectral emissivity, and the one estimated by means of the PTES algorithm, for a given couple of target temperature and water vapor concentration of the atmosphere. (c) and (d) represent the  $bias_T$  [K], in absolute value, between the actual target temperature, and the one estimated by means of the PTES algorithm, for a given couple of target temperature and water vapor concentration of the atmosphere. (e) and (f) represent the  $bias_w$  [gr/cm<sup>2</sup>], in absolute value, between the actual water vapor concentration of the atmosphere, and the one estimated by means of the PTES algorithm, for a given couple of target temperature and vapor vapor concentration of the atmosphere.

### 2.3. PTES with Atmospheric Correction



**Figure 2.14:** Aluminum-zinc sample. (a) and (b) represent the  $rmse_{\epsilon}$ , expressed in dB, between the actual spectral emissivity, and the one estimated by means of the PTES algorithm, for a given couple of target temperature and water vapor concentration of the atmosphere. (c) and (d) represent the  $bias_T$  [K], in absolute value, between the actual target temperature, and the one estimated by means of the PTES algorithm, for a given couple of target temperature and water vapor concentration of the atmosphere. (e) and (f) represent the  $bias_w$  [gr/cm<sup>2</sup>], in absolute value, between the actual water vapor concentration of the atmosphere, and the one estimated by means of the PTES algorithm, for a given couple of target temperature and vapor vapor concentration of the atmosphere.

## Chapter 2. Polynomial-fitting Temperature and Emissivity Separation

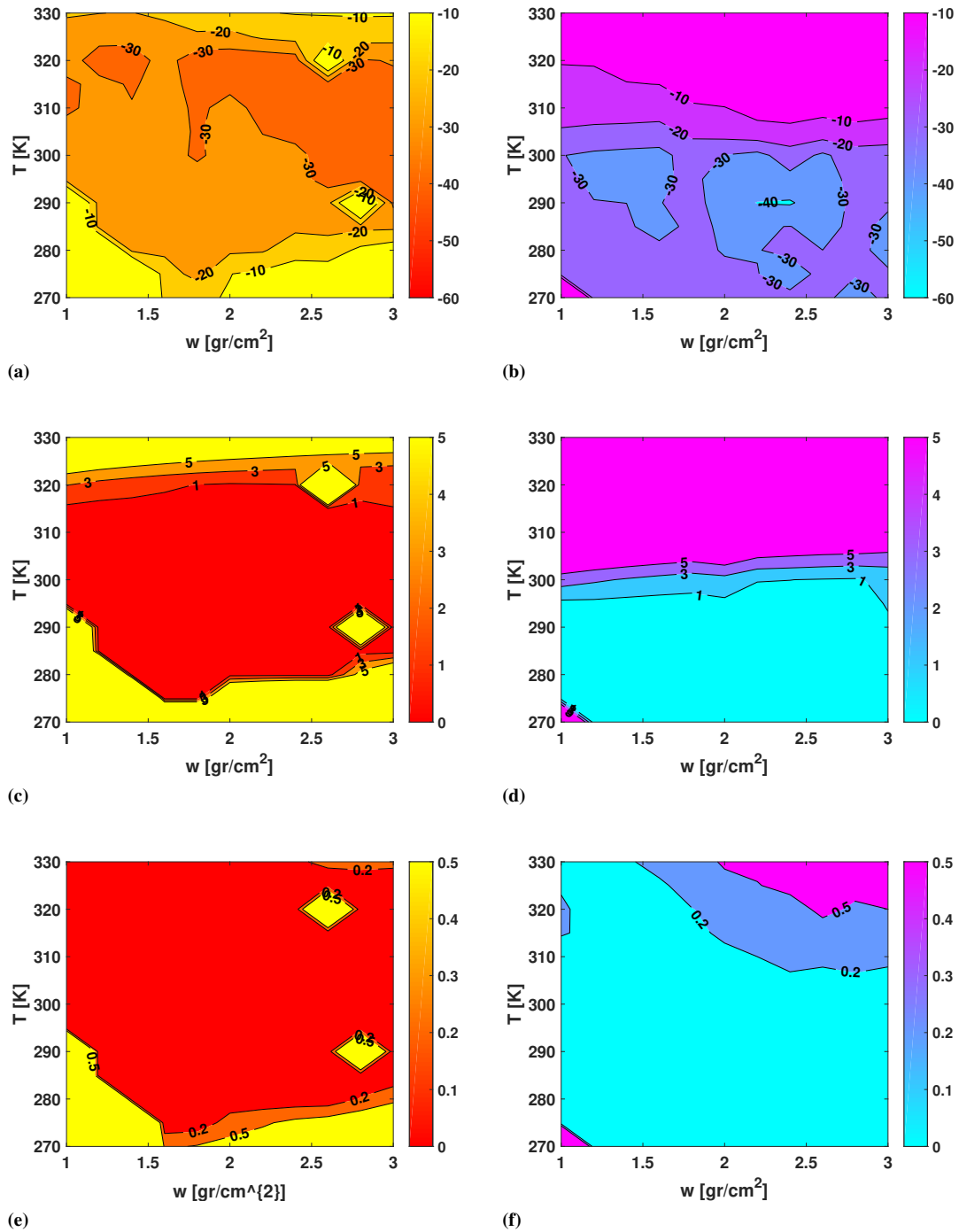


**Figure 2.15:** Aluminum sample. (a) and (b) represent the  $rmse_{\epsilon}$ , expressed in dB, between the actual spectral emissivity, and the one estimated by means of the PTES algorithm, for a given couple of target temperature and water vapor concentration of the atmosphere. (c) and (d) represent the  $bias_T$  [K], in absolute value, between the actual target temperature, and the one estimated by means of the PTES algorithm, for a given couple of target temperature and water vapor concentration of the atmosphere. (e) and (f) represent the  $bias_w$  [gr/cm<sup>2</sup>], in absolute value, between the actual water vapor concentration of the atmosphere, and the one estimated by means of the PTES algorithm, for a given couple of target temperature and vapor vapor concentration of the atmosphere.

---

## 2.4 Conclusions

---

In this chapter, a new algorithm for the TES task called Polynomial-fitting TES (PTES) has been presented. The technique has been presented in two versions. The first one suppose that the atmospheric correction of the at-sensor radiance is completely carried out by means of some AC techniques, and the downwelling spectral radiance is available. It exploits an optimization procedure, aimed to estimate the best temperature that minimizes the emission lines inside the emissivity spectral shape. The method is applied on a small spectral interval where the material signature is particularly smooth. The latter is found measuring, in different bands, the emissivity smoothness as the standard deviation of the ground-leaving radiance derivative, after an erosion-moving average filtering process. The algorithm has shown satisfactory performance on both high and low spectral emissivities, as well as the ones with high spectral dynamics. Results suggest that the mse, regardless of the emissivity value and shape, is always lower than -40 dB. Regarding the temperature estimate, the estimation errors are less than 0.5K for both high value and high spectral dynamics signatures. Instead, for the low emissivity material, the error increase to around 2K. However, the performance achieved with the PTES algorithm fulfil the requirements of mostly remote sensing applications [12, 18]. The second version is an upgrade of the PTES algorithm, that includes an atmospheric correction technique. As previously, the technique performs an optimization procedure, aimed at estimating the best target temperature and atmospheric integrated water vapour ( $w$ ) that minimize the atmospheric emission lines along the emissivity spectral shape. The latter is computed with the aid of a LUT of atmospheres, parameterized with respect to  $w$ . The evaluation procedure is performed in a spectral interval between  $8 - 8.3 \mu m$ , where most of emissivities feature a remarkable flat behaviour. The results suggest that, for summer atmosphere, the performance are generally satisfactory for temperatures included between 275K and 320K, and for  $w$  values between  $1 - 3 gr/cm^2$ , irrespective of the signatures spectral features. Instead, for a wintry atmosphere, the performance is improved, thanks to the dryer environment, thus a less radiative flux of the up/downwelling radiances. The aluminum sample features worse performance due to its low spectral emissivity that affects the self-emitted radiance, which provides disadvantages with respect to the atmospheric radiances (lower radiative transfer). Future works will investigate in depth the proposed solution open challenges, in particular the window dimension optimal choice of the filters, the sensor spectral range splitting criterion, aim to measure the smoothest spectral interval (for the first version of the algorithm), and in general the performance of both the algorithm exploiting a real data set, comparing it with the state-of-the-art techniques.

---

## Improved Alpha Residuals

---

### 3.1 Introduction

---

In Long Wave Infrared hyperspectral systems, target detection is accomplished exploiting the spectral emissivity signature [20]. Emissivity and temperature are tightly combined inside the measured radiance; their joint estimation represents a challenging task because, for the observed radiance at  $N_c$  channels, there will always be  $N_c + 1$  unknowns, i.e., the temperature and the  $N_c$  emissivity samples [12]. This problem is known in the literature as temperature–emissivity separation (TES). Many TES algorithms have been developed during the last decades [2, 7, 13, 19, 23, 24] based on different assumptions and/or constraints. Unfortunately, TES algorithms retrieve the object temperature with a limited accuracy, and errors in the retrieved object temperature generate errors in the estimated emissivity spectrum [18], reducing the performance of the subsequent detection step. To overcome this problem, some researchers have pursued methods based on ad hoc functions of the emissivity that do not depend or are only slightly influenced by the object temperature. In this framework, a promising solution was first proposed by Kealy and Gabell [28] and Kealy and Hook [29]. They derived a zero mean function of the emissivity spectrum, called alpha residuals (AR) and showed how it could be computed from the measured spectral radiance without any knowledge of the object temperature. In a target detection problem, the AR for the target of interest are computed from the emissivity spectrum in a spectral library and compared with the AR spectrum obtained from the measured radiance. The AR approach was improved by Gillespie [9], in which they proposed a more accurate method to compute the AR from the measured radiance. Namely, instead of dropping the dependence on the object temperature, they used a rough estimate of the temperature itself and derived a new expression for the AR which yielded higher accuracy than the method in [28] and [29]. The main limitation, of both the aforementioned AR approaches, is that they

ignore the contribution of the radiance emitted by the atmosphere and reflected from the viewed object. This leads to poor accuracy in the evaluation of the AR, especially for the objects with low or moderate emissivity [12], [20]. This loss of accuracy generates a difference between the reference AR spectra evaluated from the library, and the ones computed from the measured radiance, reducing the detection performance for typical targets of interest in operating scenarios. In this chapter, an improved version of the AR is proposed. The method properly takes into account the radiance emitted by the atmosphere and reflected from the ground. The proposed AR are derived by limiting as much as possible the dependence on the object temperature, and provide better accuracy than the previous methods [9, 29], both for high and low emissivity targets. For the sake of clarity, the AR are presented by expliciting the dependence of all the terms in Eq. 1.3 from the wavelength. This approach allows to propose a more easily dissertation. The paragraph is organized as follows: In Section 3.2, the AR methods proposed in [9, 29] are briefly reviewed, and an evidence of the impact of the simplifying hypothesis used to derive them is given. In Section 3.3, the new AR approach is derived. Finally, in Section 3.4, experimental results are presented and discussed.

### 3.2 Problem Statement

The AR spectrum was first introduced in [28] to automatically retrieve, from the remotely sensed radiance, a function of the object emissivity, to be used for object recognition without explicitly estimating the object temperature. Denoting with  $\epsilon(\lambda_i)$ ,  $i = 1, 2, \dots, N_c$  the object emissivity,  $\{\lambda_i\}$  being the central wavelength of the  $N_c$  sensor channels, the AR spectrum associated to  $\epsilon(\lambda_i)$  is defined as:

$$\alpha_\epsilon(\lambda_i) = \lambda_i \ln[\epsilon(\lambda_i)] - \frac{1}{N_c} \sum_{i=1}^{N_c} \lambda_i \ln[\epsilon(\lambda_i)] \quad (3.1)$$

The relationship between the AR spectrum and the measured radiance, is derived from the ground-leaving radiance  $L_{gl}(\lambda_i)$  [28], [9], which is expressed as [20]:

$$\begin{aligned} L_{gl}(\lambda_i) &= \epsilon(\lambda_i)L_{BB}(\lambda_i, T) + [1 - \epsilon(\lambda_i)]L_\downarrow(\lambda_i) = \\ &= \frac{\epsilon(\lambda_i)c_1}{\lambda_i^5 [\exp(c_2/\lambda_i T) - 1]} + [1 - \epsilon(\lambda_i)]L_\downarrow(\lambda_i) \end{aligned} \quad (3.2)$$

where:

- $L_{BB}(\lambda_i, T)$  is the radiance emitted by a blackbody at temperature  $T$
- $c_1 = 11910 \text{ W}\mu\text{m}^4\text{cm}^{-2}\text{sr}^{-1}$
- $c_2 = 14387.86 \mu\text{mK}$
- $L_\downarrow(\lambda_i)$  is the atmospheric downwelling radiance, supposed known

The ground leaving radiance is obtained by the at sensor radiance through atmospheric correction, i.e. removing the path emitted radiance and normalizing to the path transmittance [20], [21]. To briefly review the existing methods proposed to compute the AR spectrum from  $L_{gl}(\lambda_i)$ , and to pave the way for the new approach presented in

Section 3.3, the notation proposed refers to the one in [9]. For this purpose, in Eq. 3.2 the term  $L_{\downarrow}(\lambda_i)$  is neglected, and let  $k_i = 48/\lambda_i$ ,  $C(k_i) = c_1/\lambda_i^5$ ,  $t = 300/T$ , to obtain:

$$L_{gl}(k_i) = \epsilon(k_i) \frac{C(k_i)}{e^{k_i t} - 1} \quad (3.3)$$

Notice that, for the sake of clarity, the dependence of radiometric quantities on the wavelength may be denoted with  $k_i$  or  $\lambda_i$  according to the context, hereinafter. Given a function  $x(k_i)$ ,  $i = 1, 2, \dots, N_c$  the following operator is defined:

$$T_{\alpha}[x(k_i)] \triangleq \frac{48 \ln x(k_i)}{k_i} - \frac{48}{N_c} \sum_{i=1}^{N_c} \frac{\ln x(k_i)}{k_i} \quad (3.4)$$

which it is may call the  $\alpha$  operator, because one can easily see that  $T_{\alpha}[\epsilon(k_i)]$  returns the AR spectrum  $\alpha_{\epsilon}(\lambda_i)$  defined in Eq. 3.1 with the change of variable  $k_i = 48/\lambda_i$ . Applying  $T_{\alpha}[\bullet]$  to Eq. 3.3 and rearranging the terms one has:

$$T_{\alpha}[\epsilon(k_i)] = T_{\alpha}[L_{gl}(k_i)] - T_{\alpha}[C(k_i)] + T_{\alpha}[e^{k_i t} - 1] \quad (3.5)$$

As already noted, the left-hand side of Eq. 3.5 corresponds to the AR spectrum  $\alpha_{\epsilon}(\lambda_i)$  defined in Eq. 3.1 and, in a typical object detection application can be computed from the object emissivity taken from a spectral library. Instead, the right-hand side of Eq. 3.5, denoted hereinafter as  $\hat{\alpha}_{\epsilon}(k_i, t)$ , suggests how the AR can be computed from the measured radiance. In practice, the computation of  $\hat{\alpha}_{\epsilon}(k_i, t)$  requires the knowledge of the object temperature which is not available. To overcome this problem, two different approaches have been proposed in the literature. In the first approach [28, 29], the Wien's approximation is used and the "-1" term is neglected in the last term in Eq. 3.5. This simplification removes the dependence on the temperature term  $t = 300/T$ , leading to the following expression:

$$\hat{\alpha}_W(k_i) = T_{\alpha}[L_{gl}(k_i)] - T_{\alpha}[C(k_i)] \quad (3.6)$$

where the subscript "W" denotes the Wien's approximation. A different approach was proposed in [9] where the authors exploited a 0th-order Taylor expansion with respect to the variable  $t$  around a value  $t_0 = 300/T_0$ . Using this approximation, the following expression is obtained:

$$\hat{\alpha}_T(k_i) = T_{\alpha}[L_{gl}(k_i)] - T_{\alpha}[C(k_i)] + T_{\alpha}[e^{k_i t_0} - 1] \quad (3.7)$$

where the subscript "T" now denotes the Taylor's expansion. Notice that, in this latter approach, one needs a value  $T_0$  for the object temperature, while the rationale for using the AR is to estimate a quantity related to the object spectral emissivity independent on the object temperature. However, the authors demonstrated that the temperature  $T_0$  used in Eq. 3.7 can differ significantly from the true object temperature without affecting so much the AR estimation accuracy. Namely, in [9] the authors used  $T_0 = 300$  K, and showed that, within a true temperature range of 250-350 K, Eq. 3.7 may provide better accuracy than the method based on Wien's approximation. In practice,  $T_0$  is

obtained running one of the many TES techniques to get a rough estimate of the temperature for the observed object. Since high accuracy in the temperature estimates is not required, it may be advisable to use a computationally fast TES algorithm, such as the one in [2], to reduce the computational load of the whole processing chain. Both the methods in [9, 29] have been derived from Eq. 3.3 neglecting the atmospheric effects, i.e. ignoring the influence of  $L_{\downarrow}(\lambda_i)$  in Eq. 3.2. This approximation can be considered valid only for high emissivity materials. For low emissivity materials, the reflected radiance depending on  $L_{\downarrow}(\lambda_i)$  is not negligible and may even be the dominant term in  $L_{gl}(\lambda_i)$ .

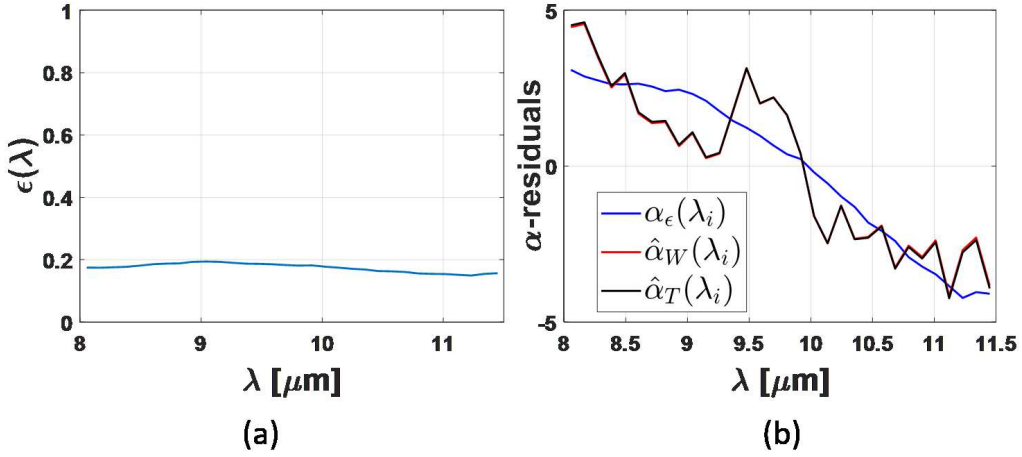


**Figure 3.1:** Effect of  $L_{\downarrow}(\lambda_i)$  on the AR, (a) aluminum emissivity, (b) AR for aluminum spectrum.

This is exemplified in Fig. 3.1 that shows the effect of the term  $L_{\downarrow}(\lambda_i)$  on the AR for a low emissivity spectrum. The figure was obtained using an aluminum spectrum taken from the Urban Micromet spectral library [30] and simulating the atmosphere and the acquisition sensor. A standard Mid-Latitude Summer atmosphere generated with MODTRAN [1] has been used, with an object temperature of 300 K. Notice that, as is shown in Fig. 3.1b, the AR spectra computed with Wien and Taylor approximations differ from the true spectrum  $\alpha_{\epsilon}(\lambda_i)$  obtained from the spectral library, and show sharp variations due to the uncompensated atmospheric term  $L_{\downarrow}(\lambda_i)$ .

### 3.3 Improved Alpha Residuals

In this section, a new approach to the alpha residuals that accounts for the dependence on  $L_{\downarrow}(\lambda_i)$  is presented.  $L_{\downarrow}(\lambda_i)$  was ignored to derive Eq. 3.6 and Eq. 3.7. For this purpose, Eq. 3.2 is written as follows:

$$L_{gl}(\lambda_i) - L_{\downarrow}(\lambda_i) = \epsilon(\lambda_i)[L_{BB}(\lambda_i, T) - L_{\downarrow}(\lambda_i)] \quad (3.8)$$

and the operator  $T_{\alpha}[\bullet]$  is applied to both sides of Eq. 3.8. After a few simple manipulations, one can easily get the following expression for the AR:

$$\hat{\alpha}_\epsilon(k_i, t) = T_\alpha [L_{gl}(k_i) - L_\downarrow(k_i)] + T_\alpha [(1 - e^{-k_i t})] + \quad (3.9)$$

$$- T_\alpha \left[ 1 - \frac{L_\downarrow(k_i)(e^{k_i t} - 1)}{C(k_i)} \right] - T_\alpha [C(k_i)]$$

As in Eq. 3.5, the dependence on  $t$  is removed assuming  $t = t_0 = 300/T_0$ , where  $T_0$  is an initial estimate of the object temperature. So, letting  $t = t_0$  in Eq. 3.9 a new expression for the AR is obtained, called  $\hat{\alpha}_{M_0}(k_i)$ , hereinafter, that accounts for  $L_\downarrow(\lambda_i)$ . Of course, if  $L_\downarrow(k_i) = 0$ ,  $\hat{\alpha}_{M_0}(k_i)$  is the same as  $\hat{\alpha}_T(k_i)$  in Eq. 3.7. It is worth noting that the approximation error:

$$\text{err}(k_i, t) \triangleq \hat{\alpha}_\epsilon(k_i, t) - \hat{\alpha}_{M_0}(k_i) = \alpha_\epsilon(k_i) - \hat{\alpha}_{M_0}(k_i) \quad (3.10)$$

made letting  $t = t_0$  in Eq. 3.9, depends on  $t$  but does not depend on the object emissivity  $\epsilon(k_i)$ . Stated in another way, given  $t$  and, of course, for a given value of  $t_0$  and  $L_\downarrow(k_i)$ , the error signal is the same whatever the object emissivity. Of course, the error is zero if the true temperature  $T$  is equal to  $T_0$ . In Eq. 3.10 has been exploited the fact that, when the true value of  $t$  is known, the AR computed from Eq. 3.9 coincide with the ones computed from the emissivity spectrum, i.e.  $\hat{\alpha}_\epsilon(k_i, t) = \alpha_\epsilon(k_i)$ . In practice,  $T_0$  is obtained by running a TES algorithm and differs from  $T$ . Typical errors expected for fast TES techniques are within the range  $\pm 5$  K [2, 18]. Thus, it is important to understand how such range of uncertainty in the object temperature influences the accuracy of the estimated AR through the error term of Eq. 3.10. For this purpose, one starts noting that,

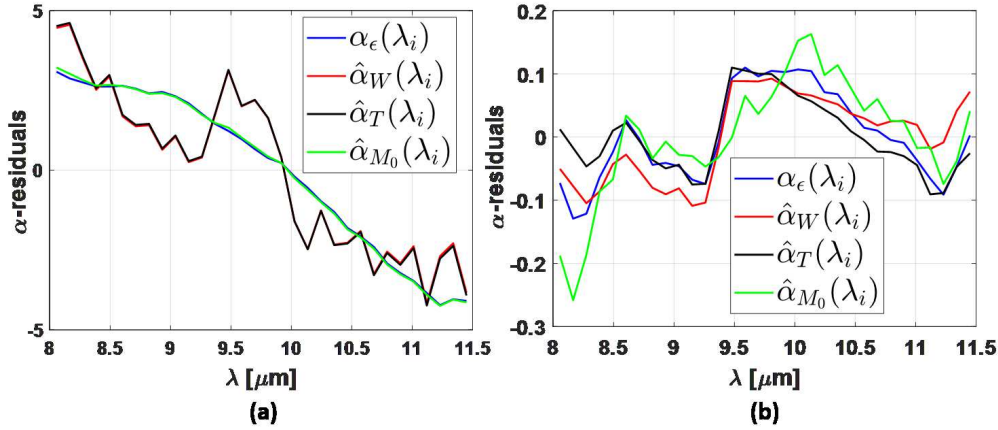


**Figure 3.2:** Effect of the approximation error on the AR;  $T - T_0 = -3$  K,  $T_0 = 300$  K,  $L_\downarrow(\lambda_i)$  the same as in Fig. 3.1. (a) low emissivity - aluminum, (b) high emissivity - asphalt.

though the error term is independent on object emissivity, its effect on the alpha residuals in Eq. 3.9 changes with  $\epsilon(k_i)$ . This is illustrated in Fig. 3.2. Fig. 3.2a shows that, for low emissivities,  $\ln \epsilon(\lambda_i)$  amplifies the spectral emissivity changes making  $\text{err}(k_i, t)$  negligible ( $\hat{\alpha}_\epsilon \simeq \hat{\alpha}_{M_0}$ ). Instead, for high emissivities, as is shown in Fig. 3.2b, the logarithm compresses the range of variation of the alpha residuals and the approximation error becomes a heavy source of distortion. Fig. 3.2 also shows

$\hat{\alpha}_W(k_i)$  and  $\hat{\alpha}_T(k_i)$  for comparison. Notice that, for high emissivity materials, and a temperature error of 3 K,  $\hat{\alpha}_W(k_i)$  and  $\hat{\alpha}_T(k_i)$ , which have been derived without taking into account  $L_\downarrow(k_i)$ , may yield better results than  $\hat{\alpha}_{M_0}(k_i)$ . Thus, since the uncertainty in the true target temperature may generate a high difference between  $\hat{\alpha}_{M_0}$  and  $\hat{\alpha}_\epsilon$ , for high emissivity values, one has to find a method to mitigate the effect of such an error source. For this purpose, a carefully study of the dependence of  $\text{err}(k_i, t)$  on the variable  $t$  is done in Eq. 3.10. Specifically, considering  $\hat{\alpha}_\epsilon(k_i, t)$  in Eq. 3.9 as a function of  $t$  and expand it in Taylor's series, around  $t = t_0$ , one obtains:

$$\text{err}(k_i, t) = \alpha_{M_1}(k_i)\Delta t + o(k_i, \Delta t^2) \quad (3.11)$$

where  $\Delta t \triangleq t - t_0$  and  $\alpha_{M_1}(k_i)$  is the first derivative of  $\hat{\alpha}_\epsilon(k_i, t)$  with respect to  $t$  computed in  $t = t_0$ :

$$\alpha_{M_1}(k_i) = T_\alpha \left[ e^{\frac{k_i}{(e^{k_i t_0} - 1)}} + \frac{k_i L(k_i) e^{k_i t_0}}{C(k_i) - L_\downarrow(k_i) (e^{k_i t_0} - 1)} \right] \quad (3.12)$$

Reminding that TES techniques provide an uncertainty on the temperature estimate of a few K, it is assumed that  $o(k_i, \Delta t^2)$  is negligible in Eq. 3.11. To support this hypothesis, in Fig. 3.3 a typical value of the ratio (dB) between the energy of  $o(k_i, \Delta t^2)$ , and the one of  $\alpha_{M_1}(k_i)\Delta t$ , as a function of  $\Delta t$  for  $T_0 = 300$  K is shown. For better clarity, the plot is quoted using a  $T$  (K) labeled axis at the bottom of the graph and showing the corresponding  $\Delta t$  values at the top.

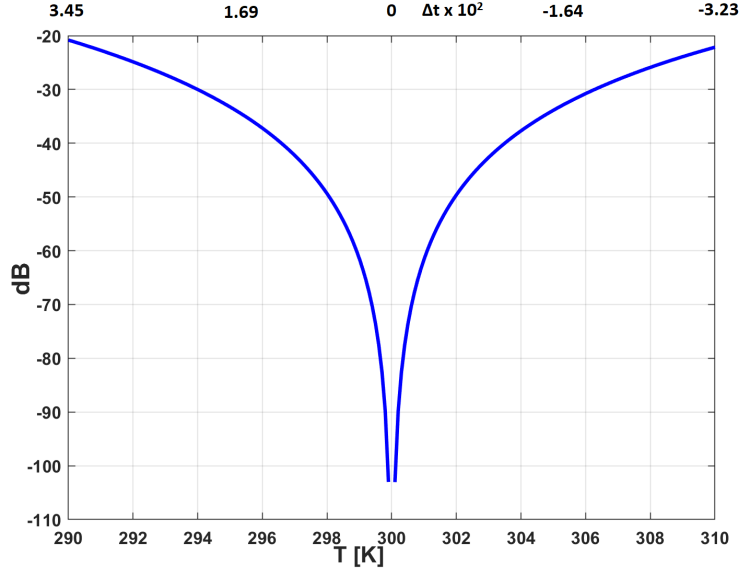


**Figure 3.3:** Ratio (dB) between the energy of  $o(k_i, t^2)$  and the one of  $\alpha_{M_1}(k_i)\Delta t$ ;  $T_0 = 300$  K

Notice that, for  $|\Delta T| = |T - T_0| \leq 10$  K the energy of  $o(k_i, \Delta t^2)$  is more than 20 dB lower than that of  $\alpha_{M_1}(k_i)\Delta t$ . Thus, one may reasonably neglect the  $o(k_i, \Delta t^2)$  term and rewrite Eq. 3.11 as:

$$\text{err}(k_i, t) = \alpha_{M_1}(k_i)\Delta t \quad (3.13)$$

Since  $L_{\downarrow}(k_i)$  is assumed known, the (first order) error term consists of the known signal  $\alpha_{M_1}(k_i)$  scaled by an unknown factor  $\Delta t$ . To improve the accuracy of the method, a way to annihilate the error term whichever be  $\Delta t$  is found. For this purpose, Eq. 3.10 is rewritten as:

$$\hat{\alpha}_{M_0}(k_i) = \alpha_{\epsilon}(k_i) - \alpha_{M_1}(k_i)\Delta t, \quad i = 1, 2, \dots, N_c \quad (3.14)$$

Denoting with  $\alpha_{\epsilon}$ ,  $\hat{\alpha}_{M_0}$  and  $\alpha_{M_1}$  the column vectors obtained from the  $N_c$  samples of the corresponding spectra in Eq. 3.14, Eq. 3.14 becomes:

$$\hat{\alpha}_{M_0} = \alpha_{\epsilon} - \alpha_{M_1}\Delta t \quad (3.15)$$

Eq. 3.15 suggests that a way to get rid of the dependence on the error term (whichever  $\Delta t$ ) is that of projecting  $\hat{\alpha}_{M_0}$  onto the subspace orthogonal to the direction of the vector  $\alpha_{M_1}$ . This fact leads to define a new AR spectrum  $\hat{\alpha}_M$  as:

$$\hat{\alpha}_M = \hat{\alpha}_{M_0} - (\hat{\alpha}_{M_0}^T \mathbf{i}_{M_1}) \mathbf{i}_{M_1} \quad (3.16)$$

where  $\mathbf{i}_{M_1}$  is the unit vector associated to  $\hat{\alpha}_{M_1}$ . The orthogonal projection method is expected to give good results in this framework. In fact, Eq. 3.12 shows that the  $\alpha_{M_1}$  vector is controlled by  $L_{\downarrow}(k_i)$ , which is a function of  $\lambda_i$  quite different from the object emissivity, which instead controls the *useful signal* in  $\hat{\alpha}_{M_0}$ . Therefore, a large fraction of the energy of the signal related to  $\epsilon$  is expected to be preserved in the orthogonal projection. This issue will be discussed further in the next section. Of course, when the proposed AR are used in an object detection problem, also the alpha residuals vector  $\alpha_{\epsilon}$  evaluated from the spectral library according to Eq. 3.1 must be projected onto the subspace orthogonal to  $\hat{\alpha}_{M_1}$  as in Eq. 3.16.

### 3.4 Experimental Results

---

The experimental analysis presented in this section has two main goals. First, it aims at quantifying the ability of the orthogonal projection in Eq. 3.16 to separate the error term from the true AR with reduced loss in the useful signal. Second, it aims at investigating the performance of the new AR comparing with the methods proposed in [28], [9]. Specifically, the performance is evaluated by measuring, as a function of  $\Delta t$ , the error between the true AR spectrum and the one estimated from the observed radiance. All the experiments have been carried out by using MODTRAN [1] to simulate realistic values of  $L_{gl}(\lambda_i)$  for a standard *Mid-Latitude Summer* atmospheric condition and a given object emissivity. In the simulation, a sensor operating in the 8-11.5  $\mu\text{m}$  spectral range with  $N_c = 32$  spectral channels corresponding to a FWHM around 100 nm is assumed, which are typical values for existing commercial airborne sensors (e.g. TASI-600 [11]). It is worth noting that the choice of the simulation setting is of relatively marginal interest in this work and the conclusions drawn are quite general and can be extended to other typical acquisition conditions.

### 3.4.1 Effectiveness of the orthogonal projection

In order to experimentally validate the heuristic intuition that the orthogonal projection, used in Eq. 3.16, annihilates the error term, preserving the useful component related to the true AR, the proposed method is applied to all the 218 emissivity spectra contained in the MODIS [33] and in the Urban Micromet spectral library. MODTRAN has been used to simulate  $L_{gl}(\lambda_i)$  as in Eq. 1.3 and to compute  $\alpha_{M_1}$  using Eq. 3.12. Then, for each spectrum in the library, the true AR spectrum is computed, generating a vector  $\alpha_\epsilon$ . Finally,  $\alpha_\epsilon$  is projected onto the subspace orthogonal to  $\alpha_{M_1}$  to obtain a new vector  $\alpha_{\epsilon_\perp}$ . The ability of the orthogonal projection to preserve the useful information is measured estimating the energy loss in dB in the projection

$$\Delta\mathcal{E} = 10 \log_{10} \left( \frac{\sum_{i=1}^{N_c} \alpha_\epsilon^2(k_i)}{\sum_{i=1}^{N_c} \alpha_{\epsilon_\perp}^2(k_i)} \right) \quad (3.17)$$

The analysis has shown that, on average,  $\Delta\mathcal{E}=0.86$  dB and that  $\Delta\mathcal{E} \leq 2.3$  dB in 99.5% of the cases. This confirms the conclusion drawn at the end of Section 3.3.

### 3.4.2 Analysis of the estimation accuracy

In order to show the performance of the proposed method, four different emissivity spectra have been selected from the Urban Micromet spectral library. The spectra, shown in Fig. 3.4, have been chosen so as to analyze both high and low emissivity materials.

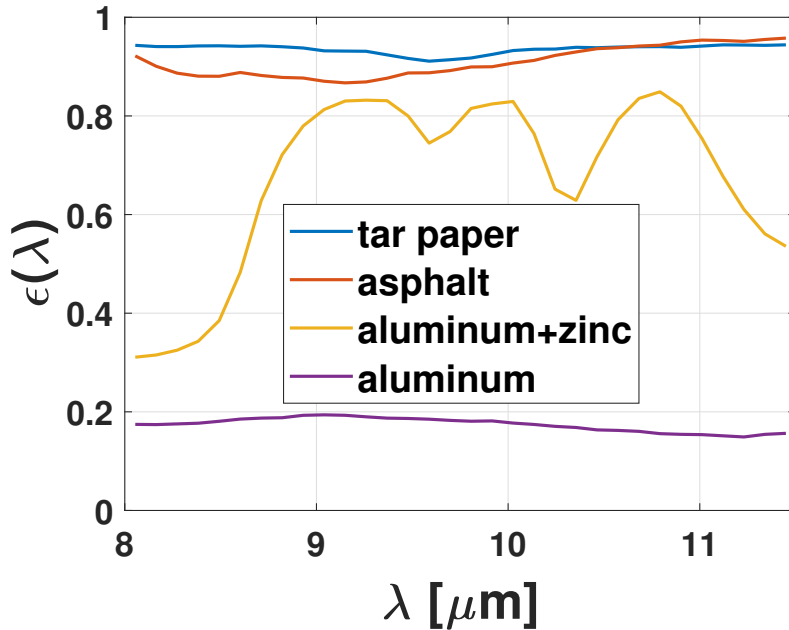


Figure 3.4: Emissivity samples

The AR estimation accuracy can be measured by estimating the difference between the alpha residuals derived from the library and those obtained from the measured radiance. For this purpose, the relative error is defined as:

$$RE = \sqrt{\frac{\sum_{i=1}^{N_c} [\alpha_\epsilon(\lambda_i) - \hat{\alpha}_x(\lambda_i)]^2}{\sum_{i=1}^{N_c} \alpha_\epsilon^2(\lambda_i)}} \quad (3.18)$$

where  $\alpha_\epsilon(\lambda_i)$  is the true AR spectrum obtained from a spectral library and  $\hat{\alpha}_x(\lambda_i)$ , with  $x = "W", "T"$  or  $"M"$ , is the in-scene AR obtained with one of the three aforementioned techniques.

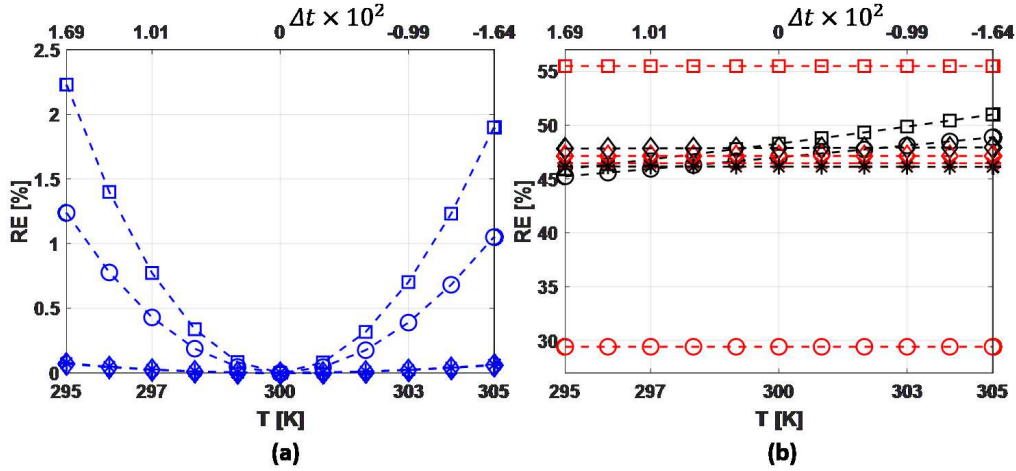
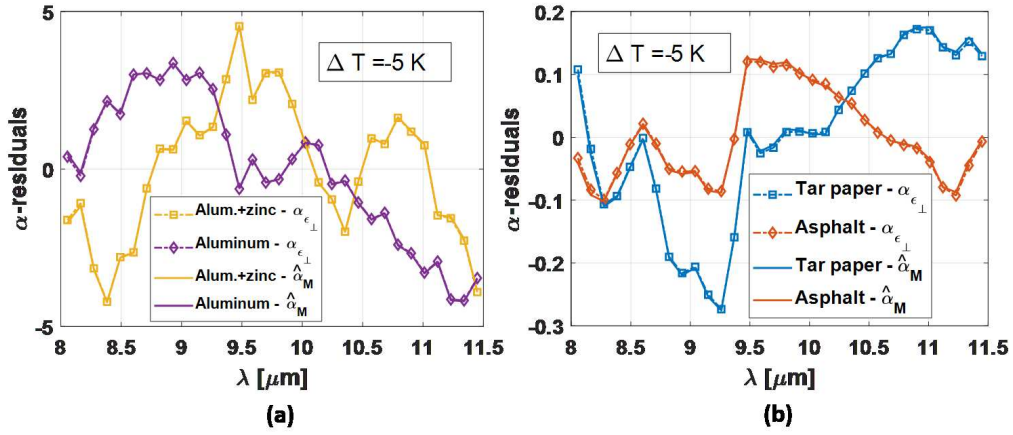


Figure 3.5: Residual error as a function of  $\Delta t$  ( $T_0 = 300$  K)

Fig. 3.5 shows the RE as a function of  $T$  (and  $\Delta t$ ) for the three methods and the four emissivity spectra shown in Fig. 3.4 and was obtained assuming  $T_0 = 300$  K. The different methods have been coded with different colors: blue for "M", red for "W" and black for "T". Similarly, the markers are associated to the different emissivity spectra: "circle" for tar paper, "square" for asphalt, "diamond" for aluminum+zinc and "asterisk" for aluminum. For better clarity, the different y-axis scale are managed using two different subfigures. Fig. 3.5a refers to  $\hat{\alpha}_M$  while Fig. 3.5b to  $\hat{\alpha}_W$  and  $\hat{\alpha}_T$ . The figure shows that, in all cases, the proposed method outperforms the methods based on Wien and Taylor approximations, which always have unacceptable performance with RE above or close to 30%. To better discuss the results obtained with the new method one has to separate the two cases of high (asphalt and tar paper) and low/medium (aluminum and aluminum+zinc) emissivity. One may easily notice that for low emissivity materials the RE obtained with the  $\hat{\alpha}_M$  residuals has a very low dependence on  $\Delta t$  while, for high emissivities, the dependence on  $\Delta t$  is more evident though it leads to RE below 2.5% in the worst case (i.e.  $\Delta T = -5$  K). As discussed in Section 3.3, this result is explained reminding that the approximation error is the same for every spectrum but has a lower impact over low emissivity materials. Actually, this apparently disappointing different performance for high and low emissivities is not critical in practice. In fact, if the temperature  $T_0$  is estimated with an accurate TES method such as [23], the temperature error is usually in the range of  $\pm 3$  K for both high and low emissivity materials, thus leading to RE below 1% in all the cases. Otherwise, as advisable in this application, if one uses a computationally fast TES algorithm [2], the temperature estimate is quite accurate for high emissivity samples (below 1 K as claimed in [2]) while, for low

emissivity materials, the estimate error may sensibly increase. The good news is that for low emissivity materials, as is depicted in Fig. 3.5, the RE is less sensitive to  $\Delta t$ . As to the Wien and Taylor methods, Fig. 3.5b shows that neglecting  $L_{\downarrow}(\lambda_i)$  leads to unacceptable performance with relative errors always close or higher than 30%. Notice that  $\hat{\alpha}_W(k_i)$  do not depend on  $\Delta t$ , so the red curves are horizontal lines whose values depend only on the object emissivity. As expected, for low emissivity samples, the RE is higher because when  $\epsilon(\lambda_i)$  decreases, the reflected component  $[1 - \epsilon(\lambda_i)]L_{\downarrow}(\lambda_i)$  in Eq. 3.2 increases and neglecting it results in a gross approximation that leads large errors in the estimated AR. As far as  $\hat{\alpha}_T(\lambda_i)$  is concerned, the dependence of RE on  $\Delta t$  is indeed scarcely appreciable in Fig. 3.5b, in compliance with the results in [9]. However, Fig. 3.5b also shows that, different from what obtained in [9], where the analysis was carried out ignoring the  $[1 - \epsilon(\lambda_i)]L_{\downarrow}(\lambda_i)$  contribution in Eq 3.2, the Wien approximation may yield lower errors than the Taylor expansion based approach.



**Figure 3.6:** Comparison between  $\hat{\alpha}_M$  and  $\alpha_{\epsilon_{\perp}}$ : (a) low emissivity materials, (b) high emissivity materials;  $\Delta T = -5K$ .

This section is concluded comparing, in Fig. 3.6,  $\hat{\alpha}_M$  (solid line) and  $\alpha_{\epsilon_{\perp}}$  (dot-dash line with markers) for the materials shown in Fig. 3.4. For better clarity, the curves have been sketched for low (aluminum+zinc and aluminum) and high (tar paper and asphalt) emissivity materials using two different figures to manage the different y-axis scale. The figure was obtained with  $\Delta T = -5 K$  to illustrate how, in the worst case, the RE values in Figure 3.5a affect the computation of the AR. Fig. 3.6 shows that the  $\hat{\alpha}_M$  and  $\alpha_{\epsilon_{\perp}}$  curves are practically coincident for low emissivity materials, while their difference is quite small for high emissivity materials. The improvement obtained with the orthogonal projection can be easily appreciated comparing the result shown in Fig. 3.2b for the asphalt with the one in Fig. 3.6b. Though Fig. 3.2b was obtained with  $\Delta T = -3 K$  the difference between  $\hat{\alpha}_{M_0}$  and  $\alpha_{\epsilon}$  is much higher than that between  $\hat{\alpha}_M$  and  $\alpha_{\epsilon_{\perp}}$  in Fig. 3.6b. The improvement can be quantified using the RE: in Fig. 3.2b the RE was 69% for  $\hat{\alpha}_{M_0}$  while using the new approach RE = 0.8% for the asphalt is obtained, with  $\Delta T = -3 K$  and RE = 2.3% with  $\Delta T = -5K$ .

In Table 3.1 the RE% for  $\hat{\alpha}_M$  with  $\Delta T = -3K$  and  $-5K$  are compared with the RE% for the  $\hat{\epsilon}$  in Fig. 3.4 and their estimates obtained by inverting (1.3). The Table shows that RE% for  $\hat{\alpha}_M$  is always much lower than the one obtained from  $\hat{\epsilon}$ . This result is

$\Delta T$	Tar paper		Asphalt		Aluminum+Zinc		Aluminum	
	$\hat{\alpha}_M$	$\hat{\epsilon}$	$\hat{\alpha}_M$	$\hat{\epsilon}$	$\hat{\alpha}_M$	$\hat{\epsilon}$	$\hat{\alpha}_M$	$\hat{\epsilon}$
-3K	0.44	6.3	0.8	6	0.025	6	0.026	6
-5K	1.3	10.4	2.3	10.4	0.07	9.97	0.08	10.5

**Table 3.1:** RE% for  $\hat{\alpha}_M$  and  $\hat{\epsilon}$

quite promising for target detection applications where the spectra of objects of interest (taken from a library) are compared with the ones estimated from the observed radiance.

### 3.5 Conclusions

---

In this paragraph, a new method to compute alpha residuals that improves state of art approaches [9,28] have been presented. The method takes into account the contribution of the radiance emitted by the atmosphere and reflected by the viewed object. Experimental analysis, carried out with simulated data, has shown the better accuracy of the new AR, and its poor sensitivity to  $\Delta t$  when the temperature estimate errors assume typical values. The new AR approach is expected to provide good results in target detection applications where an initial rough guess of the temperature, maybe provided by a fast TES algorithm, allows the AR computation procedure to get a *spectrum*, related to the object emissivity, which can be reliably employed for spectral matching.

#### Appendix: derivation of Eq. 3.9

---

Starting from Eq. 3.8, the natural logarithm is applied to both sides of the equation. The term that contains the spectral emissivity is isolated:

$$\ln [\epsilon (\lambda_i)] = \ln [L_{gl} (\lambda_i) - L_{\downarrow} (\lambda_i)] - \ln [L_{BB} (\lambda_i, T) - L_{\downarrow} (\lambda_i)] \quad (3.19)$$

Then, a change of variable from  $\lambda_i$  to  $k_i$  is applied to Eq. 3.19. Further, both sides of the equation are multiplied for  $48/k_i$ :

$$\frac{48}{k_i} \ln [\epsilon (k_i)] = \frac{48}{k_i} \ln [L_{gl} (k_i) - L_{\downarrow} (k_i)] - \frac{48}{k_i} \ln [L_{BB} (k_i, T) - L_{\downarrow} (k_i)] \quad (3.20)$$

In order to make the problem easily treatable, Eq. 3.20 is rewritten as follows:

$$A(k_i) = B(k_i) - D(k_i) \quad (3.21)$$

For each term of Eq. 3.21, the mean value is subtracted:

$$A(k_i) - \bar{A}(k_i) = \frac{48}{k_i} \ln [\epsilon (k_i)] + \frac{48}{N_c} \sum_{i=1}^{N_c} \frac{\ln [\epsilon (k_i)]}{k_i} \triangleq T_{\alpha} [\epsilon (k_i)] \triangleq \alpha_{\epsilon} (k_i, t) \quad (3.22)$$

$$\begin{aligned}
 B(k_i) - \bar{B}(k_i) &= \frac{48}{k_i} \ln [L_{gl}(k_i) - L_{\downarrow}(k_i)] + \\
 -\frac{48}{N_c} \sum_{i=1}^{N_c} \frac{\ln [L_{gl}(k_i) - L_{\downarrow}(k_i)]}{k_i} &\triangleq T_{\alpha} [L_{gl}(k_i) - L_{\downarrow}(k_i)]
 \end{aligned} \tag{3.23}$$

$$\begin{aligned}
 D(k_i) - \bar{D}(k_i) &= \frac{48}{k_i} \ln \left[ \frac{C(k_i)}{e^{k_i t} - 1} - L_{\downarrow}(k_i) \right] + \\
 -\frac{48}{N_c} \sum_{i=1}^{N_c} \frac{\ln \left[ \frac{C(k_i)}{e^{k_i t} - 1} - L_{\downarrow}(k_i) \right]}{k_i} &
 \end{aligned} \tag{3.24}$$

In Eq. 3.24, the transformation in Eq. 3.3 has been used. Further, in Eq. 3.24 the property of the logarithm is then exploited:

$$\begin{aligned}
 D(k_i) - \bar{D}(k_i) &= \frac{48}{k_i} \ln \left[ \frac{C(k_i)}{e^{k_i t} - 1} \right] + \frac{48}{k_i} \ln \left[ 1 - \frac{L_{\downarrow}(k_i) (e^{k_i t} - 1)}{C(k_i)} \right] + \\
 -\frac{48}{N_c} \sum_{i=1}^{N_c} \frac{\ln \left[ \frac{C(k_i)}{e^{k_i t} - 1} \right]}{k_i} - \frac{48}{N_c} \sum_{i=1}^{N_c} \frac{\ln \left[ 1 - \frac{L_{\downarrow}(k_i) (e^{k_i t} - 1)}{C(k_i)} \right]}{k_i} &
 \end{aligned} \tag{3.25}$$

Then, applying again the property of the logarithm, and recognized the  $\alpha$ -operator, one obtain:

$$\begin{aligned}
 D(k_i) - \bar{D}(k_i) &= \frac{48}{k_i} \ln [C(k_i)] - \frac{48}{k_i} \ln [e^{k_i t} - 1] + \\
 +T_{\alpha} \left[ 1 - \frac{L_{\downarrow}(k_i) (e^{k_i t} - 1)}{C(k_i)} \right] - \frac{48}{N_c} \sum_{i=1}^{N_c} \frac{\ln [C(k_i)]}{k_i} + \frac{48}{N_c} \sum_{i=1}^{N_c} \frac{\ln [e^{k_i t} - 1]}{k_i} &
 \end{aligned} \tag{3.26}$$

In Eq. 3.26, the  $\alpha$ -operator is again recognized:

$$\begin{aligned}
 D(k_i) - \bar{D}(k_i) &= T_{\alpha} [C(k_i)] + T_{\alpha} \left[ 1 - \frac{L_{\downarrow}(k_i) (e^{k_i t} - 1)}{C(k_i)} \right] + \\
 -\frac{48}{k_i} \ln [e^{k_i t} - 1] + \frac{48}{N_c} \sum_{i=1}^{N_c} \frac{\ln [e^{k_i t} - 1]}{k_i} &
 \end{aligned} \tag{3.27}$$

After an easy manipulation of Eq. 3.27, one obtain:

$$\begin{aligned}
 D(k_i) - \bar{D}(k_i) &= T_\alpha [C(k_i)] + T_\alpha \left[ 1 - \frac{L_\downarrow(k_i) (e^{k_i t} - 1)}{C(k_i)} \right] + \\
 &\quad - T_\alpha [1 - e^{-k_i t}] - 48t + \frac{48t}{N_c} \sum_{i=1}^{N_c} 1 = \quad (3.28) \\
 &= T_\alpha [C(k_i)] + T_\alpha \left[ 1 - \frac{L_\downarrow(k_i) (e^{k_i t} - 1)}{C(k_i)} \right] - T_\alpha [1 - e^{-k_i t}]
 \end{aligned}$$

Finally, recomposing Eq. 3.22, Eq. 3.23, and Eq. 3.28, Eq. 3.9 is correctly obtained.

If  $L_\downarrow(k_i) = 0$ , from Eq. 3.9 one obtain:

$$\alpha_\epsilon(k_i, t) = T_\alpha [L_{gl}(k_i)] - T_\alpha [C(k_i)] + T_\alpha [1 - e^{-k_i t}] \quad (3.29)$$

Thus, basically Eq. 3.29 is rewritten as:

$$\ln [\epsilon(k_i)] = \ln [L_{gl}(k_i)] - \ln [C(k_i)] + \ln [1 - e^{-k_i t}] + \ln [e^{k_i t}] \quad (3.30)$$

The last term of Eq. 3.30 must be added due to the simplification done in Eq. 3.28. Thus, exploiting the properties of the logarithm, at the end one obtain:

$$\epsilon(k_i) \frac{C(k_i)}{e^{k_i t} - 1} = \epsilon(k_i) L_{BB}(k_i, t) = L_{gl}(k_i) \quad (3.31)$$

---

## Subspace-based Target Detection

---

### 4.1 Introduction

---

In hyperspectral systems applications, target detection is accomplished exploiting the spectral signature of the target-of-interest (TOI) [16]. In the last decades, the visible (VIS), and near-infrared (NIR) domains have been deeply investigated, and several works have been published regarding this task. More recently, the scientific community has focused its attention on long-wave infrared (LWIR) hyperspectral systems and their application to target detection problems. Such systems allow day and night operations, and give the possibility to estimate the target temperature [20]. The works published in this field commonly exploit the hypothesis that the atmosphere is known, or can be obtained by some estimation techniques [3, 4, 14, 27]. In the literature, the process of estimating the atmosphere is commonly split in two steps. The first step is *atmospheric correction*, which consists in estimating the ground leaving radiance by removing the contributions due to the spectral transmittance and upward radiance (or path radiance). The second step consists in estimating the downward spectral radiance (or downwelling radiance) [20]. Being related to the atmosphere between the target and the sensor, the spectral transmittance and upward radiance may be estimated exploiting ancillary data obtained from a weather balloon, in conjunction with a computer code such as MODTRAN [1]. Furthermore, they may be estimated directly from the remotely-sensed data, by methods such as the In-Scene Atmospheric Correction (ISAC) algorithm [10,32], the Autonomous Atmospheric Compensation method (AAC) [9], or the recently proposed Coupled Subspace-Based Atmospheric Compensation (CSAC) [21]. The downward spectral radiance is obviously related to both the transmittance and upward radiance, but it is not directly deducible from them, being produced by the elements of the entire atmospheric column from ground to space [20]. In general, the estimate of the downward radiance is difficult because a down-looking sensor cannot acquire knowledge of

the atmosphere above the platform, especially for low-altitude collections such as those made by airborne sensors. A valuable solution was proposed in [17], by exploiting the ground leaving radiance from low emissivity pixels and combining a temperature emissivity separation (TES) algorithm with a downwelling radiance look-up table.

In this chapter, a new forward-modeling (FM) full-pixel target detection algorithm is presented. The method takes into account for the downwelling radiance spectral variability by means of a subspace-based model. FM based target detection was investigated within the VNIR-SWIR spectral domain [5] but it has not been yet extended to the LWIR domain. In this domain, the problem is complicated by the non-linear dependence of the pixel spectral radiance on the surface temperature. In FM target detection, the TOI spectral emissivity is transformed into a TOI spectral radiance by means of an atmospheric radiation transfer model, and by specifying the model parameters on the basis of atmospheric and viewing conditions at the acquisition time [22]. The proposed approach requires neither knowledge of the temperature of the target nor the accurate knowledge of the downwelling radiance vector. It is based on the assumption that this vector belongs to a subspace having rank lower than the number of spectral channels. This chapter is organized as follows. In Section 4.2, the new target detection algorithm is presented. In Section 4.3, the simulation strategy, applied to provide an evidence of the effectiveness of the proposed algorithm, is discussed. Finally, in Section 4.4 experimental results obtained on simulated data are shown.

## 4.2 Algorithm Description

---

In this chapter, the focus is on the following problem: for each pixel of a LWIR hyperspectral image one have to decide if the surface corresponding to that pixel is composed of the material with known spectral emissivity  $\bar{\epsilon}$ . It can be formulated as a *one-class classification* problem where, by observing a given ground-leaving radiance vector  $\mathbf{L}_{g1}$ , we have to decide if it is due to a surface having the known TOI emissivity spectrum (denoted as  $\bar{\epsilon}$ , hereinafter) or not.

Such a problem can be solved by a fitting-based approach, where the observed spectral radiance  $\mathbf{L}_{g1}$  is compared with its model reconstruction, obtained according to Eq. 1.3, and with the value of the emissivity spectrum that we want to detect. Specifically, we use the Relative Error (RE) defined as:

$$\text{RE} [\bar{\epsilon}, T, \mathbf{L}_{\downarrow}] = \frac{\|\mathbf{L}_{g1} - \hat{\mathbf{L}}_{g1}(\bar{\epsilon}, T, \mathbf{L}_{\downarrow})\|_2}{\|\mathbf{L}_{g1}\|_2} \quad (4.1)$$

In Eq. 4.1,  $\|\cdot\|_2$  denotes the  $l_2$ -norm and  $\hat{\mathbf{L}}_{g1}(\bar{\epsilon}, T, \mathbf{L}_{\downarrow})$  is the reconstruction of  $\mathbf{L}_{g1}$  obtained exploiting the model in Eq. 1.3 by setting  $\epsilon = \bar{\epsilon}$ .  $\text{RE} [\bar{\epsilon}, T, \mathbf{L}_{\downarrow}]$  measures how well the model fit the current observation. The presence of the TOI is decided if the statistics RE is lower than a given threshold.

It is worth nothing that, in Eq. 4.1, it is implicitly assumed that both  $T$  and  $\mathbf{L}_{\downarrow}$  are known. Such hypothesis is not realistic, and both the variables must be replaced with their estimates obtained by the observed  $\mathbf{L}_{g1}$ . The problem of estimating  $T$  and  $\mathbf{L}_{\downarrow}$  by the observed  $\mathbf{L}_{g1}$  (supposing  $\epsilon$  to be known) is ill-posed, because the number of unknowns ( $N_c + 1$ ) is greater than the number of observation ( $N_c$ ). Thus, following an approach similar to the one adopted in [23], it is assumed that the vectors  $\mathbf{L}_{\downarrow}$  span a

linear subspace having a rank  $K$  lower than  $N_c$ . Specifically, denoting as  $\mathbf{U}$  the  $N_c \times K$  basis matrix of such a subspace,  $\mathbf{L}_\downarrow$  can be expressed as:

$$\mathbf{L}_\downarrow = \mathbf{U}\mathbf{a} \quad (4.2)$$

where  $\mathbf{a}$  is the  $K \times 1$  vector of the coefficients of  $\mathbf{L}_\downarrow$  with respect to the basis  $\mathbf{U}$ . Assuming as known the basis  $\mathbf{U}$ , the unknowns in Eq. 4.1 become  $T$  and  $\mathbf{a}$ . According to the introduced subspace model, the fitting problem is reformulated so as to have  $K + 1$  unknowns with  $N_c$  observations, with  $K + 1 < N_c$ :

$$\text{RE} [\bar{\epsilon}, T, \mathbf{a}] = \frac{\|\mathbf{L}_{\text{gl}} - \hat{\mathbf{L}}_{\text{gl}}(\bar{\epsilon}, T, \mathbf{a})\|_2}{\|\mathbf{L}_{\text{gl}}\|_2} \quad (4.3)$$

$T$  and  $\mathbf{a}$ , that minimize the previous equation, are obtained by the following minimization problem:

$$\begin{bmatrix} \hat{T} \\ \hat{\mathbf{a}} \end{bmatrix} = \arg \min_{\vartheta \in [T_{LB}, T_{UB}]} \text{RE} [\bar{\epsilon}, \vartheta, \boldsymbol{\alpha}] \quad (4.4)$$

$\boldsymbol{\alpha}$

The minimization in Eq. 4.4 is performed choosing  $\boldsymbol{\alpha}$  within  $\mathbb{R}^{K \times 1}$ , and by varying  $\vartheta$  between a minimum ( $T_{LB}$ ) and a maximum ( $T_{UB}$ ) temperature, set on the basis of the characteristics of the monitored scene. To solve the problem, it is proposed to first minimize RE with respect to the vector  $\boldsymbol{\alpha}$ , and then search for the best estimate of  $\vartheta$  as follows:

$$\begin{bmatrix} \hat{T} \\ \hat{\mathbf{a}} \end{bmatrix} = \arg \min_{\vartheta \in [T_{LB}, T_{UB}]} \left[ \min_{\boldsymbol{\alpha}} \text{RE} [\bar{\epsilon}, \vartheta, \boldsymbol{\alpha}] \right] \quad (4.5)$$

It is worth noting that, observing the signal model in Eq. 1.3, given a guess of the target temperature  $\vartheta$ , the optimum estimate of  $\mathbf{a}$  is obtained from the observed radiance as least square solution of Eq. 4.5 as follows:

$$\hat{\mathbf{a}}(\vartheta) = \mathbf{U}^+ \mathbf{L}_\downarrow^{\text{inv}}(\vartheta) \quad (4.6)$$

where  $\mathbf{U}^+$  is the pseudo-inverse matrix of  $\mathbf{U}$ , and  $\mathbf{L}_\downarrow^{\text{inv}}(\vartheta)$  is

$$\mathbf{L}_\downarrow^{\text{inv}}(\vartheta) = [\mathbf{I} - \mathbf{D}_{\bar{\epsilon}}]^{-1} [\mathbf{L}_{\text{gl}} - \mathbf{D}_{\bar{\epsilon}} \mathbf{L}_{\text{BB}}(\vartheta)] \quad (4.7)$$

Substituting Eq. 4.6 inside Eq. 4.5, the problem is rewritten with the target temperature as the only unknown parameter:

$$\hat{T} = \arg \min_{\vartheta \in [T_{LB}, T_{UB}]} \text{RE} [\bar{\epsilon}, \vartheta, \hat{\mathbf{a}}(\vartheta)] \quad (4.8)$$

that can be solved by resorting to an easy algorithm.  $\text{RE} [\bar{\epsilon}, \hat{T}, \hat{\mathbf{a}}(\hat{T})]$  is the statistic for the detection task. If lower than a given threshold, detection is declared.

An experimental evidence of the goodness of the subspace model assumption for  $\mathbf{L}_\downarrow$ , along with a possible strategy to obtain the basis matrix  $\mathbf{U}$ , are given in Sub-Section 4.2.1.

### 4.2.1 Determination of the Basis Matrix $\mathbf{U}$

To estimate the basis matrix  $\mathbf{U}$ , an approach similar to the one adopted in [21] is followed. First, MODTRAN is exploited to construct a dictionary of spectral downwelling radiances  $\mathbf{D}$ , parameterized with respect to the variation of the *total column water vapor*  $w$  (also known as *integrated water vapor*) within a given interval. Then, the low-rank basis matrix  $\mathbf{U}$  is extracted from such a dictionary. To extract  $\mathbf{U}$ , it is exploited that the idea that in the portion of the LWIR spectral range, the variability of the dictionary members  $\mathbf{d}_p$  (with  $p = 1, \dots, P$ ) can be well represented on a subspace having a rank  $K < N_c$ , that is

$$\mathbf{d}_p \simeq \mathbf{U}\mathbf{b} \quad \forall p = 1, \dots, P \quad (4.9)$$

where  $P$  is the number of dictionary members,  $\mathbf{d}_p$  is the  $p^{\text{th}}$  dictionary member,  $\mathbf{U}$  is the basis matrix of such a subspace, and  $\mathbf{b}$  is the vector of the components of  $\mathbf{d}_p$  on the basis  $\mathbf{U}$ . The matrix  $\mathbf{U}$  may be obtained by using the Singular Value Decomposition (SVD) algorithm, i.e. retaining the singular vectors that best represent the data in the maximum power sense [15, 21, 23].

In order to give an example of the effectiveness of the proposed procedure, the integrated water vapor interval  $[0.5 - 3.5] \text{ gr/cm}^2$  is considered, based on the information of the AERONET database [25], for a standard mid-latitude summer atmosphere. Furthermore, as example, it is considered the Hyperspectral Thermal Emission Spectrometer (HyTES), that is an airborne imaging spectrometer with 256 spectral channels between  $7.5\mu\text{m}$  and  $12\mu\text{m}$ , with a full-width at half-maximum of  $35\text{nm}$  and a spectral sampling of  $17\text{nm}$  [26]. Generally, the bands affected by strong atmospheric absorption are discarded. In this case, the bands from  $11.5$  to  $12\mu\text{m}$  have been neglected. The resulting number of spectral bands is  $N_c = 202$ .

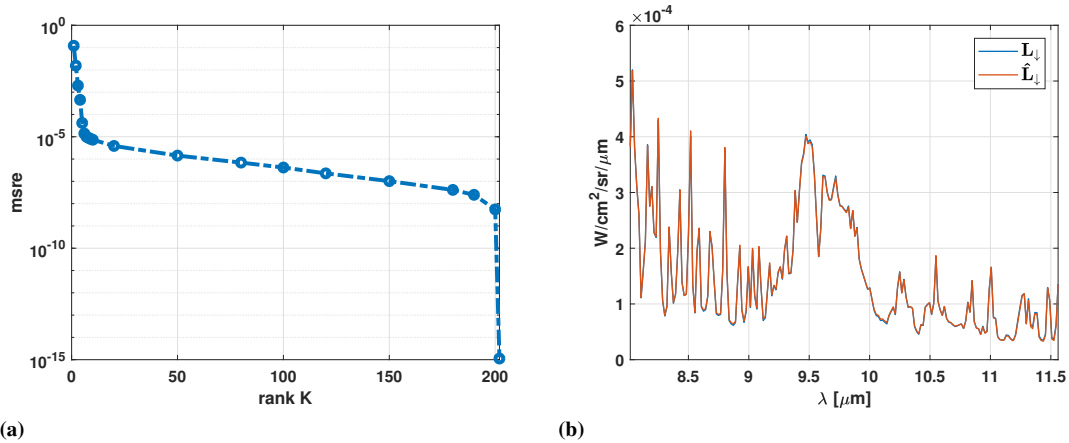


**Figure 4.1:** (a) Subspace reconstruction of  $\mathbf{L}_\downarrow$  as a function of  $K$ . (b) Comparison between  $\mathbf{L}_\downarrow$  and its worst low-rank reconstruction for  $K = 3$

Fig. 4.1a shows the subspace reconstruction of  $\mathbf{L}_\downarrow$ , in terms of mean square relative error (msre), defined as the ratio between the  $l_2$ -norm of the reconstruction error and the  $l_2$ -norm of  $\mathbf{L}_\downarrow$ , as a function of the rank of the matrix  $\mathbf{U}$ . In this case, the number of dictionary members used to estimate the basis matrix is  $P = 6000$ . For each assessed

rank, the number of water vapor samples  $w$ , within the considered interval, is 1000. Fig. 4.1a shows that the effective subspace spanned by  $L_{\downarrow}$  is indeed very low, being the msre lower than  $10^{-3}$  at  $K = 4$ . Fig. 4.1b shows the true and the estimated value of  $L_{\downarrow}$  obtained with  $K = 3$  and for the value of  $w$  that produced the worst rmse, equal to  $4 \cdot 10^{-3}$ . Despite the small rank used in this example, the two curves are practically coincident.

Without loss of generality, standard information about the  $\text{CO}_2$ ,  $\text{O}_3$ , aerosol and temperature profiles, commonly available within the MODTRAN environment, have been used. The generalization of the technique to a more complex combination of unknown atmospheric elements is out of the scope of this thesis.

### 4.3 Simulation Strategy

In order to prove the effectiveness of the proposed detection technique, an evaluation of its performance, in terms of Receiver Operating Characteristics (ROC), on simulated data is provided. For this purpose, for a given TOI with spectral emissivity  $\bar{\epsilon}$ , two different sets of at-sensor radiance spectra are generated:  $H_1$  and  $H_0$ .  $H_1$  is the set of the at-sensor radiance spectra simulating the target present hypothesis, i.e. with reference to the RTM in Eq. 1.2 and 1.3 they are generated by setting  $\epsilon = \bar{\epsilon}$ .  $H_0$  is the set of radiances corresponding to the target absent hypothesis and are obtained using for  $\epsilon$  values other than  $\bar{\epsilon}$ . The proposed algorithm is applied to  $H_1$  and  $H_0$ , varying the detection threshold, in order to obtain the detection probability ( $P_D$ ) and the false alarm probability ( $P_{FA}$ ), respectively. Performance in terms of ROC curves are shown and discussed in Section 4.4. The simulation strategy, adopted in this Section, is outlined in Fig. 4.2

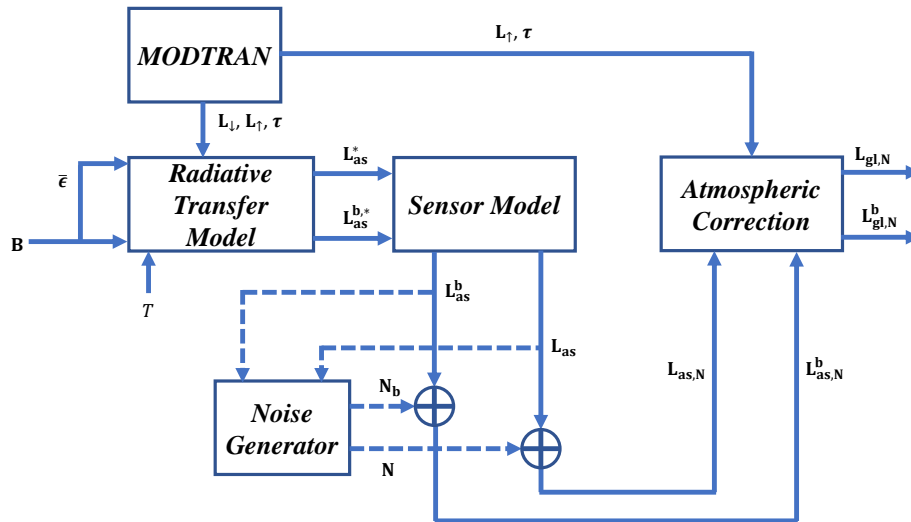


Figure 4.2: Block diagram of the simulation strategy

In order to simulate the data set  $H_1$ , a TOI emissivity spectrum  $\bar{\epsilon}$  is extracted from the database  $B$ , obtained by merging the open-access MODIS [33] and Urban Micromet [30] spectral libraries. Such  $\bar{\epsilon}$  is combined with the radiometric quantities  $\tau$ ,

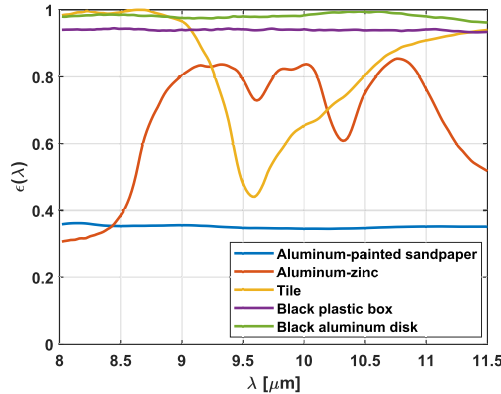


Figure 4.3: Materials used for the experimental simulations

$\mathbf{L}_{\uparrow}$ , and  $\mathbf{L}_{\downarrow}$  generated by MODTRAN and with a temperature value  $T$  according to the RTM in Eq. 1.2 and 1.3, in order to obtain the at-sensor radiance spectrum  $\mathbf{L}_{\text{as}}^* \in H_1$ .  $\tau$ ,  $\mathbf{L}_{\uparrow}$ , and  $\mathbf{L}_{\downarrow}$  are generated by assuming a nadir-view from an airplane with a flight altitude of 1Km. The atmospheric parameters setting, with the exception of the integrated water vapor  $w$ , is that of the standard mid-latitude summer MODTRAN model.  $w$  is drawn from a uniform distribution in the interval  $[0.5 - 3.5] \text{ gr/cm}^2$ . The temperature  $T$  is drawn from a uniform distribution in the interval  $[T_0 - \Delta_T, T_0 + \Delta_T]$ , with  $T_0 = 35^\circ\text{C}$  and  $\Delta_T = 15^\circ\text{C}$ . The generated  $\mathbf{L}_{\text{as}}^*$  are properly transformed in the sensor spectral domain ( $\mathbf{L}_{\text{as}}$ ) accounting for the Hyperspectral Thermal Emission Spectrometer (HyTES) sensor specifications [26]. To make more realistic the simulated radiance, a Gaussian noise with zero mean and diagonal covariance matrix is added to  $\mathbf{L}_{\text{as}}$  to obtain the noisy at-sensor radiance vector  $\mathbf{L}_{\text{as},N}$ . Noise is simulated as suggested in [21] setting the Noise Equivalent Delta Temperature (NEDT). Varying  $w$ ,  $T$  and the noise realizations,  $M = 10^3$  different  $\mathbf{L}_{\text{as},N}$  vectors are simulated to obtain the  $H_1$  data set. The same procedure is adopted to simulate the noisy at sensor radiance spectra  $\mathbf{L}_{\text{as},N}^b$  in the data set  $H_0$ . For this purpose, all the spectra in the database  $\mathbf{B}$  are used, except for  $\bar{\epsilon}$  (TOI).

In order to derive the ROC curves, the detection algorithm is applied to each element of the two data sets after removing the contributions of  $\tau$  and  $\mathbf{L}_{\uparrow}$ , thus obtaining the ground leaving radiance spectra [21]. Of course, the algorithm is applied by using  $\bar{\epsilon}$  as TOI spectral emissivity.

#### 4.4 Experimental Results

Five experiments have been carried out by considering five different materials as TOIs. The emissivity spectra  $\bar{\epsilon}$  for each of the TOI adopted in the experiments are shown in Fig. 4.3. Those five materials are chosen to test the algorithm with respect to TOI spectra with different features, such as high and low mean value and spectral variability.

In all the experiments the basis matrix  $\mathbf{U}$ , for the downwelling radiance subspace, is estimated from  $\mathbf{D}$ , according to the SVD-based procedure in Section 4.2.1. Specifically, setting an estimation-accuracy threshold for  $\mathbf{L}_{\downarrow}$  of  $10^{-3}$ , a rank 3 basis matrix  $\mathbf{U}$  is obtained. To analyze the impact of noise on the detection performance, different noise

levels are considered by setting  $NEDT = 0K$  (noise-free),  $NEDT = 0.1K$  (low noise level),  $NEDT = 0.2K$  (moderate noise level), and  $NEDT = 0.3K$  (high noise level).

Fig. 4.4 shows the ROC curves for three evaluated materials: aluminum-painted sandpaper, black aluminum disk, and black plastic box. Since there were no false alarms, the ROC curves for tile and aluminum-zinc are not shown. Thanks to their spectral variability, both the materials are always detected against the simulated background spectra.

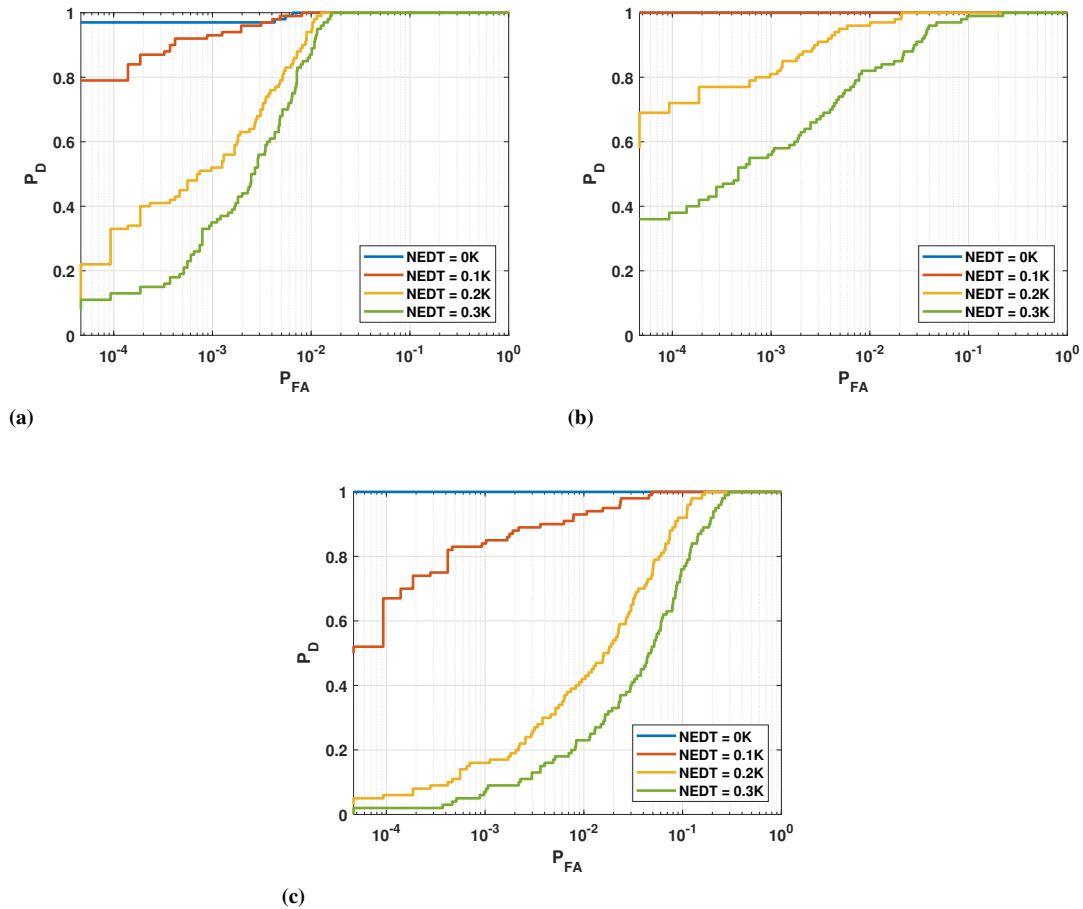


**Figure 4.4:** ROC curves: (a) aluminum-painted sandpaper; (b) black aluminum disk; (c) black plastic box

As expected, the performance increase with the decrease of the noise level. At  $NEDT = 0K$ , the three materials are substantially always detectable respect to the simulated background. The worse performance are obtained for the black plastic box. This material has been selected as "worst case", for its completely flat spectral shape (Fig. 4.3). In fact, the strategy to merge two databases that has been followed is generally a pessimistic approach. Intentionally, no distinction between the materials has been done within the dataset supposing that, in a hypothetical scenario, all the available spectra have the same probability of presentation. The dataset contains emissivities belonging to the same class of material, i.e. they have similar spectral features. In a real scenario, those spectra would be detected as target.

In order to further assess the effectiveness of the proposed target detection technique, the performance of the algorithm supposing the complete knowledge of  $\mathbf{L}_\downarrow$  has been computed. The latter represents the best case of the method, being the temperature  $T$  now the single unknown of the fitting problem described in Eq. 4.1. The related ROC curves are presented in Fig. 4.5. Of course, the performance are higher compared to the results of Fig. 4.4. However, the improvement are not substantially as expected.

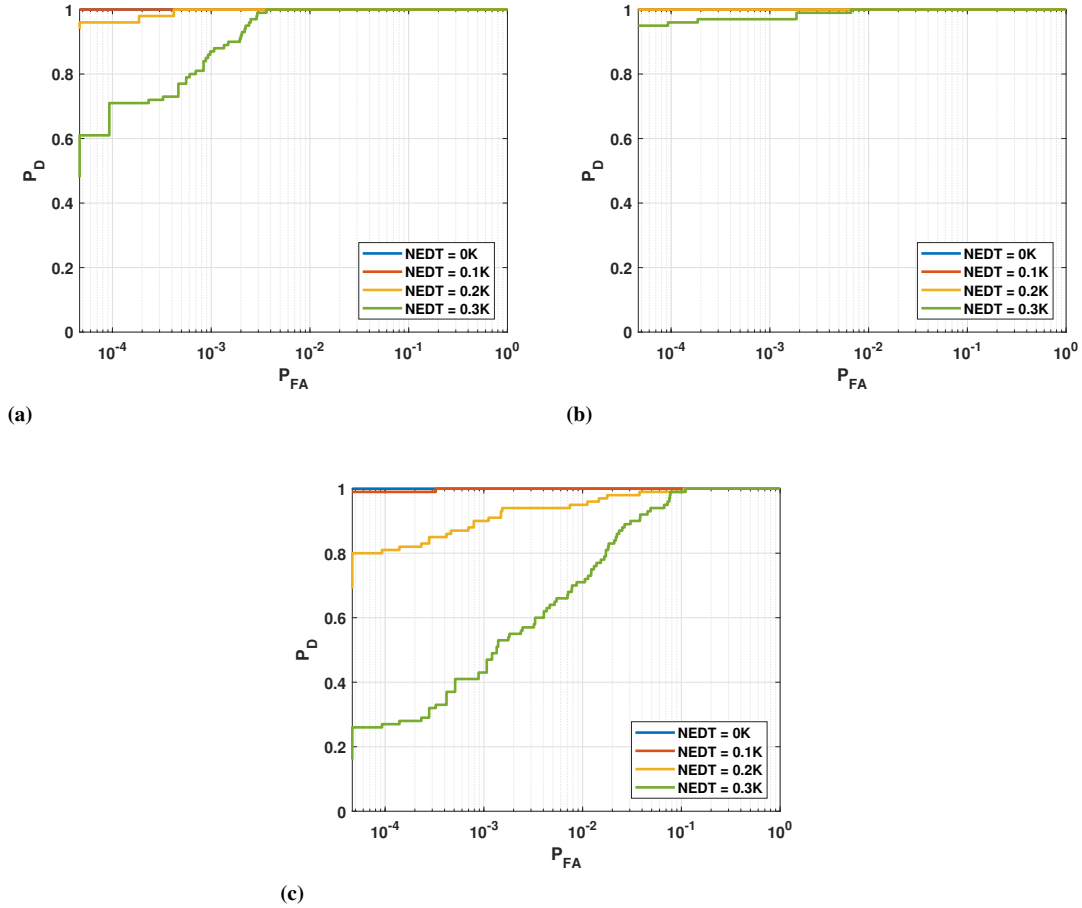


**Figure 4.5:** ROC curves with complete knowledge of  $\mathbf{L}_\downarrow$ : (a) aluminum-painted sandpaper; (b) black aluminum disk; (c) black plastic box

TABLE 4.1 summarizes the results of the ROC curves in Fig. 4.4 and 4.5, for two case studies. In the first case, at NEDT = 0.1K and fixed probability of false alarm equal to  $10^{-3}$ , the performance loss, here defined as the difference between the two probabilities of detection, is always lower than 0.15. In the second case, at NEDT = 0.2K and probability of false alarm equal to  $10^{-2}$ , the performance loss is lower than 0.05 for aluminum-painted sandpaper and black aluminum disk. Instead, for black plastic box, the loss is 0.43. For the latter material, the performance degradation at high noise value was expected, being the emissivity completely flat, i.e., easy to confuse with the simulated background materials.

The proposed algorithm may be exploited with thermal hyperspectral sensors that feature a lower number of spectral channels. In order to assess the capabilities of the

$P_D$	Aluminum-painted sandpaper		Black aluminum disk		Black plastic box	
	known $L_{\downarrow}$	$\hat{L}_{\downarrow}$	known $L_{\downarrow}$	$\hat{L}_{\downarrow}$	known $L_{\downarrow}$	$\hat{L}_{\downarrow}$
NEDT = 0.1K $P_{FA} = 10^{-3}$	1	0.95	1	1	1	0.85
NEDT = 0.2K $P_{FA} = 10^{-2}$	1	0.98	1	0.96	0.92	0.43

**Table 4.1:** Probabilities of detection for the three materials, in case of known and estimated downwelling radiance, for two case studies:  $NEDT = 0.1K$  and  $P_{FA} = 10^{-3}$ , and  $NEDT = 0.2K$  and  $P_{FA} = 10^{-2}$

detection technique, further tests have been performed by simulating the TASI-600 hyperspectral sensor responsivity [11]. As already introduced in Chapter 3, it features  $N_c = 32$  spectral channels corresponding to a FWHM around 100 nm, within the 8-11.5  $\mu\text{m}$  spectral range.

As previously, the basis matrix  $\mathbf{U}$ , for the downwelling radiance subspace, is estimated from  $\mathbf{D}$ , according to the SVD-based procedure in Section 4.2.1. Specifically, setting again an estimation-accuracy threshold for  $L_{\downarrow}$  of  $10^{-3}$ , a rank 3 basis matrix  $\mathbf{U}$  is obtained. To analyze the impact of noise on the detection performance, two noise levels are considered:  $NEDT = 0K$  (noise-free), and  $NEDT = 0.1K$  (low noise level).

Fig. 4.6 shows the ROC curves for the previously evaluated three materials: aluminum-painted sandpaper, black aluminum disk, and black plastic box. Since there were no false alarms, again the ROC curves for tile and aluminum-zinc are not shown. Although the lower number of spectral channels, their spectral variability allow both the materials to be always detected against the simulated background spectra. At  $NEDT = 0K$ , the three materials are can be always recognized with respect to the simulated "background". At  $NEDT = 0.1K$ , as expected, the worse performance are featured as previously for the black plastic box, due to its completely flat spectral shape (Fig. 4.3). However, for probability of false alarm  $P_{FA} = 5 \cdot 10^{-2}$ , black aluminum disk and aluminum-painted sandpaper feature a unitary probability of detection  $P_D$ , and black plastic box features a  $P_D \simeq 0.9$ , proving the effectiveness of the proposed algorithm.

It is worth noting that the choice of the sensor characteristics, in terms of spectral responsivity, is of relatively marginal interest and the conclusions drawn are quite general and can be extended to other typical hyperspectral imagers. Nevertheless, being the performance quite sensitive to the noise level, the choice of the sensor must be driven by the  $NEDT$ .

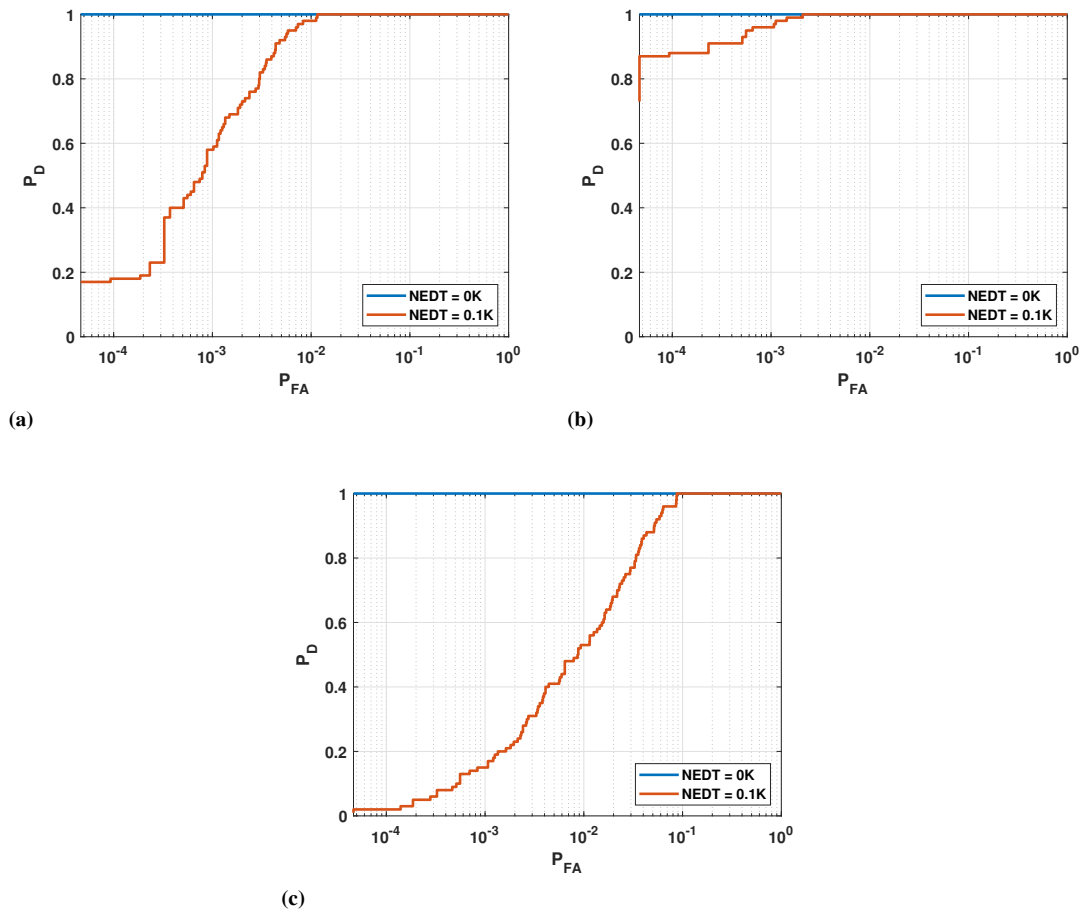


**Figure 4.6:** ROC curves (TASI-600 sensor): (a) aluminum-painted sandpaper; (b) black aluminum disk; (c) black plastic box

---

**4.5 Conclusions**

---

In this chapter, a new full-pixel target detection technique for longwave infrared hyperspectral images has been presented. The proposed method takes into account the spectral variability of the downwelling radiance, that is modeled by means of a subspace-based approach. Experimental analysis, carried out with simulated data, has shown that the algorithm may detect with high performance materials whose emissivity exhibits high spectral variability. Instead, detection performance with materials whose emissivities has low spectral variability, is sensibly affected by the noise level. However, for moderate noise levels, the technique presents performance comparable with the one obtained when the downwelling radiance is known.

Although it would be interesting to extend our analysis to real thermal infrared hyperspectral data, we are unable to do so because of the lack of appropriate experimental data sets. Currently, simulation is the only tool to analyze the performance of the algorithm, and get reliable conclusions in realistic scenarios, while having the control and full knowledge of each important parameter.

---

# CHAPTER 5

---

## Conclusions of the Thesis

---

The work presented in this dissertation attempts to propose a novel signal processing chain, aimed to exploit data acquired by long wave infrared (LWIR) hyperspectral sensors. The long wave infrared radiation from an object is directly related to its temperature, i.e. hotter the surface of the target, higher the emitted electromagnetic energy. As shown throughout the thesis, two main challenging tasks affect the development and the deployment of thermal hyperspectral sensors:

- *atmospheric correction*: the process of estimate and compensate the thermal radiation produced by the atmosphere, that affects the thermal radiation produced by the target.
- *temperature emissivity separation*: the joint estimate of the target temperature and spectral emissivity represents an ill-posed problem: given the thermal radiation of the target, measured at  $N_c$  different channels of the deployed hyperspectral sensor, the unknowns of the problem are  $N_c + 1$ , i.e. the  $N_c$  spectral sample of its emissivity, and the temperature.

In this framework, multiple aspects and arguments may be investigated and developed. The thesis has been focused on the development of a signal processing chain, optimized for the task of *target detection*, i.e. recognize a given material within a complex remote sensing scenario.

The dissertation has been structured in three main chapters:

- **Polynomial-fitting Temperature and Emissivity Separation**: the chapter concerns about the problem of temperature and emissivity separation from the remotely-sensed spectral radiance of the target. The section is divided in two main parts: first, the problem has been treated supposing that the atmospheric correction of

---

the at-sensor radiance is completely carried out. The proposed algorithm solves the TES indeterminateness exploiting an optimization procedure, by estimating the best temperature that minimizes the atmospheric-residuals features inside the emissivity spectral shape. Then, the temperature is estimated within a small spectral interval where the emissivity is smooth. In order to measure the signature smoothness in several intervals, an erosion-moving average filtering procedure is applied to the ground leaving radiances.

In the second part of the section, an improvement of the algorithm is proposed. Being the atmospheric correction a not easy processing task, due to the uncertainties of the atmosphere itself, a Look-up-Table (LUT) of plausible atmospheres is provided as input of the algorithm. The latter are obtained with the aid of the software MODTRAN, based on assumptions regarding the predicted atmosphere of the remote sensing scenario.

- **Improved Alpha Residuals:** the chapter proposes a new technique to compute the alpha residuals (AR). The technique describes a method to transfer the spectral radiance captured by the hyperspectral sensor into a new *spectrum*, that is weakly dependent by the target temperature. The computed spectrum can be used to perform a target detection task. The proposed method improves existing approaches taking into account the contribution of the atmospheric emitted radiance reflected by the target surface.
- **Subspace-based Target Detection:** the chapter presents a new method to perform the detection of materials with known spectral emissivity. The proposed approach differs from existing methods because it takes into account the uncertainty of the downwelling radiance. The technique assumes that the downwelling radiance spans a low-rank subspace whose basis matrix is learned, regardless of the analyzed image, from MODTRAN simulated spectra.

The thesis has investigated in details the logical branch addressed to target detection. However, the applications of the proposed signal processing chain may be the more disparate, from environmental remote sensing (climate change, volcanos monitoring, gas and waste pollution etc.) to defence and surveillance purposes. The latter applications may be of primary interesting for future developments and works regarding the hyperspectral remote sensing and signal processing in the LWIR spectral domain.

---

---

## Bibliography

---

- [1] A. Berk. Modtran5: 2006 update. *Proc. SPIE*, 6233, 2006.
- [2] A. Gillespie, S. Rokugawa, T. Matsunaga, S. Cothorn, S. Hook, A. B. Kahle. A temperature and emissivity separation algorithm for advanced spaceborne thermal emission and reflection radiometer (aster) images. *IEEE Trans. Geosci. Remote Sens.*, 36(4):1113–1126, 1998.
- [3] B. Ranking, J. Meola, D. Perry, J. Kaufman. Methods and challenges for target detection and material identification for longwave infrared hyperspectral imagery. *Algorithms and Technologies for Multispectral, Hyperspectral, and Ultraspectral Imagery XXII*, 2016.
- [4] B. Ranking, J. Meola, M. T. Eismann. Spectral radiance modeling and bayesian model averaging for long-wave infrared hyperspectral imagery and subpixel target identification. *IEEE Trans. Geosci. Remote Sens.*, 55(12):6726–6735, 2017.
- [5] B. Thai, G. Healey. Invariant subpixel material detection in hyperspectral imagery. *IEEE Trans. Geosci. Remote Sens.*, 40 (3):599–608, 2002.
- [6] C. C. Borel. Surface emissivity and temperature retrieval for hyperspectral sensor. *Proc. Geosci. and Remote Sens. Symp., Seattle, WA, USA*, 1998.
- [7] C. C. Borel. Artemiss - an algorithm for retrieve temperature and emissivity from hyper-spectral thermal image data. *28th Annual GOMACTech Conference, Hyperspectral Imaging Session, Tampa, FL*, (technical report LA-UR-027907), 2003.
- [8] D. Gu, A. Gillespie, A. Kahle, F. Palluconi. Autonomous atmospheric compensation (aac) of high resolution hyperspectral thermal infrared remote-sensing imagery. *IEEE Trans. Geosci. Remote Sens.*, 38(6):2557–2570, 2000.
- [9] D. Gu, A. R. Gillespie. A new approach for temperature and emissivity separation. *Int. J. Remote Sensing*, 21(10):2127–2132, 2000.
- [10] F. Soleimani, M. Akhoondzadeh, H. Ghanbari. Improved isac algorithm to retrieve atmospheric parameters from hypes hyperspectral images using gaussian mixture model and error ellipse. *IEEE Geosci. Remote Sens. Letters*, 14(11):2087–2091, 2017.
- [11] Itres Ltd. *TASI-600*, 2019. available online at <http://www.itres.com/tasi-600/>.
- [12] J. Ahlberg. Optimizing object, atmosphere, and sensor parameters in thermal hyperspectral imagery. *IEEE Trans. Geosci. Remote Sens.*, 55 (2):658–670, 2017.
- [13] J. Cheng, S. Liang, J. Wang, X. Li. A stepwise refining algorithm of temperature and emissivity separation for hyperspectral thermal infrared data. *IEEE Trans. Geosci. Remote Sens.*, 48(3):1588–1597, 2010.
- [14] J. Levesque, E. Puckrin, P. Lahaie , C. Turcotte. Detection of unexploded ordnance using airborne lwir emissivity signature. *Proc. IEEE Int. Geosci. Remote Sens. Symp. (IGARSS)*, pages 5071–5074, 2015.
- [15] J. M. Bioucas-Dias, J. M. P. Nascimento. Hyperspectral subspace identification. *IEEE Trans. Geosci. Remote Sens.*, 46(8):2435–2445, 2008.

- [16] M. Diani, M. Moscadelli, G. Corsini. Improved alpha residuals for target detection in thermal hyperspectral imaging. *IEEE Geosci. Remote Sens. Letters*, 15(5):779–783, 2018.
- [17] M. Pieper, D. Manolakis, E. Truslow, T. Cooley, M. Brueggeman, J. Jacobson and A. Weisner. In-scene lwir downwelling radiance estimation. *Proc. SPIE 9976, Imaging Spectrometry XXI*, 99760E, 2016.
- [18] M. Pieper, D. Manolakis, E. Truslow, T. Cooley, M. Brueggeman, J. Jacobson and A. Weisner. Performance limitations of temperature-emissivity separation techniques in long-wave infrared hyperspectral imaging applications. *SPIE Opt. Eng.*, 56(8):081804–1–081804–11, 2017.
- [19] M. Pivovarnik, S. J. S. Khalsa, J. C. Jimenez-Munoz, F. Zemek. Improved temperature and emissivity separation algorithm for multispectral and hyperspectral sensors. *IEEE Trans. Geosci. Remote Sens.*, 55(4):1944–1953, 2017.
- [20] M. T. Eismann. *Hyperspectral Remote Sensing*. SPIE-Press, 2012.
- [21] N. Acito and M. Diani and G. Corsini. Coupled subspace-based atmospheric compensation of lwir hyperspectral data. *IEEE Trans. Geosci. Remote Sens.*, 57(8):5224–5238, 2019.
- [22] N. Acito, G. Corsini, M. Diani, S. Matteoli, A. Riccobono, A. Rossi. Validation of forward modeling target detection approach on a new hyperspectral data set featuring an urban scenario and variable illumination conditions. *Proc. IEEE Int. Geosci. Remote Sens. Symp. (IGARSS)*, pages 5075–5078, 2015.
- [23] N. Acito, M. Diani, G. Corsini. Subspace-based temperature and emissivity separation in lwir hyperspectral data. *IEEE Trans. Geosci. Remote Sens.*, 57(3):1523–1537, 2019.
- [24] N. Wang, H. Hu, F. Nerry, C. Li, Z.L. Li. Temperature and emissivity retrievals from hyperspectral thermal infrared data using linear spectral emissivity constraint. *IEEE Trans. Geosci. Remote Sens.*, 49(4):1291–1303, 2011.
- [25] NASA. *AERONET*, 2019. available online at <https://aeronet.gsfc.nasa.gov>.
- [26] NASA. *HyTES*, 2019. available online at <https://trs.jpl.nasa.gov/handle/2014/42293>.
- [27] P. Lahaie, J. Levesque. Sub-pixel target detection in lwir hyperspectral imagery using ground leaving radiance. *Proc. IEEE Int. Geosci. Remote Sens. Symp. (IGARSS)*, pages 4436–4439, 2015.
- [28] P. S. Kealy, A. R. Gabell. Estimation of emissivity and temperature alpha coefficients. *Proc. 2nd TIMS Wksh. JPL Pub*, pages 90–95, 1990.
- [29] P. S. Kealy, S. J. Hook. Separating temperature and emissivity in thermal infrared multispectral scanner data: Implications for recovering land surface temperatures. *IEEE Trans. Geosci. Remote Sens.*, 31(6):1155–1164, 1993.
- [30] S. Kotthaus, T. E. L. Smith, M. J. Wooster, C. S.B. Grimmond. Derivation of an urban materials spectral library through emittance and reflectance spectroscopy. *ISPRS Journal of photogrammetry and remote sensing*, 94:194–212, 2014.
- [31] S. Matteoli, M. Diani, G. Corsini. A tutorial overview of anomaly detection in hyperspectral images. *IEEE Aerospace and Electronics Systems Magazine*, 25 (8):5–28, 2010.
- [32] S. Young, B. Johnson, J. Hackwell. An in-scene method for atmospheric compensation of thermal hyperspectral data. *Journal of Geophysical Research*, 107(6):14–1–14–20, 2002.
- [33] UCBS University. *MODIS*, 2019. available online at <https://icess.eri.ucsb.edu/modis/EMIS/html/em.html>.

---

## List of Figures

---

1.1	Comparison between Sun and Earth electromagnetic radiations represented as blackbodies at 6000K and 300K, respectively . . . . .	2
1.2	Illustration of the tensor representation of a hyperspectral image . . . . .	3
1.3	Graphical representation of the signal model for an airborne acquisition . . . . .	6
2.1	Effect of an erroneous temperature estimate on the emissivity retrieval (signal model inversion of Eq. 1.3 . . . . .	10
2.2	Effects of the erosion-filtering procedure. (a) aluminum-zinc spectral emissivity. (b) $\mathbf{L}_{\mathbf{g}1}$ and its eroded (red) and eroded-filtered (black) versions . . . . .	11
2.3	Spectral signatures used for the simulations . . . . .	12
2.4	Result for asphalt sample . . . . .	13
2.5	Result for green-painted metal . . . . .	14
2.6	Result for aluminum-zinc sample . . . . .	14
2.7	Result for aluminum sample . . . . .	15
2.8	Effects of a wrong estimate of $T$ and $w$ . . . . .	16
2.9	Spectral emissivities of the class "quartzite" . . . . .	17
2.10	rmse between the actual spectral emissivity, and the one obtained by means of the PTES algorithm, in the case that the algorithm is applied within the 8-9 $\mu\text{m}$ spectral band, for a standard atmosphere with a water vapor concentration of 0.5 $\text{gr}/\text{cm}^2$ . The minimum value of the rmse is obtained when the atmospheric correction is performed exploiting the entry of the LUT at the actual water vapor concentration . . . . .	18
2.11	The figure presents the same result of Fig. 2.10, but performing the algorithm in a smaller spectral interval: 8-8.3 $\mu\text{m}$ . . . . .	18
2.12	Spectral emissivities of the selected materials chosen for the experiments . . . . .	19
2.13	Asphalt sample. (a) and (b) represent the $\text{rmse}_\epsilon$ , expressed in dB, between the actual spectral emissivity, and the one estimated by means of the PTES algorithm, for a given couple of target temperature and water vapor concentration of the atmosphere. (c) and (d) represent the $\text{bias}_T$ [K], in absolute value, between the actual target temperature, and the one estimated by means of the PTES algorithm, for a given couple of target temperature and water vapor concentration of the atmosphere. (e) and (f) represent the $\text{bias}_w$ [ $\text{gr}/\text{cm}^2$ ], in absolute value, between the actual water vapor concentration of the atmosphere, and the one estimated by means of the PTES algorithm, for a given couple of target temperature and vapor vapor concentration of the atmosphere. . . . .	22

2.14	Aluminum-zinc sample. (a) and (b) represent the $\text{rmse}_\epsilon$ , expressed in dB, between the actual spectral emissivity, and the one estimated by means of the PTES algorithm, for a given couple of target temperature and water vapor concentration of the atmosphere. (c) and (d) represent the $\text{bias}_T$ [K], in absolute value, between the actual target temperature, and the one estimated by means of the PTES algorithm, for a given couple of target temperature and water vapor concentration of the atmosphere. (e) and (f) represent the $\text{bias}_w$ [ $\text{gr}/\text{cm}^2$ ], in absolute value, between the actual water vapor concentration of the atmosphere, and the one estimated by means of the PTES algorithm, for a given couple of target temperature and vapor concentration of the atmosphere. . . . .	23
2.15	Aluminum sample. (a) and (b) represent the $\text{rmse}_\epsilon$ , expressed in dB, between the actual spectral emissivity, and the one estimated by means of the PTES algorithm, for a given couple of target temperature and water vapor concentration of the atmosphere. (c) and (d) represent the $\text{bias}_T$ [K], in absolute value, between the actual target temperature, and the one estimated by means of the PTES algorithm, for a given couple of target temperature and water vapor concentration of the atmosphere. (e) and (f) represent the $\text{bias}_w$ [ $\text{gr}/\text{cm}^2$ ], in absolute value, between the actual water vapor concentration of the atmosphere, and the one estimated by means of the PTES algorithm, for a given couple of target temperature and vapor concentration of the atmosphere. . . . .	24
3.1	Effect of $L_\downarrow(\lambda_i)$ on the AR, (a) aluminum emissivity, (b) AR for aluminum spectrum. . . . .	29
3.2	Effect of the approximation error on the AR; $T - T_0 = -3\text{ K}$ , $T_0 = 300\text{ K}$ , $L_\downarrow(\lambda_i)$ the same as in Fig. 3.1. (a) low emissivity - aluminum, (b) high emissivity - asphalt. . . . .	30
3.3	Ratio (dB) between the energy of $o(k_i, t^2)$ and the one of $\alpha_{M_1}(k_i)\Delta t$ ; $T_0 = 300\text{ K}$ . . . . .	31
3.4	Emissivity samples . . . . .	33
3.5	Residual error as a function of $\Delta t$ ( $T_0 = 300\text{ K}$ ) . . . . .	34
3.6	Comparison between $\hat{\alpha}_M$ and $\alpha_{\epsilon_\perp}$ : (a) low emissivity materials, (b) high emissivity materials; $\Delta T = -5\text{ K}$ . . . . .	35
4.1	(a) Subspace reconstruction of $\mathbf{L}_\downarrow$ as a function of $K$ . (b) Comparison between $\mathbf{L}_\downarrow$ and its worst low-rank reconstruction for $K = 3$ . . . . .	42
4.2	Block diagram of the simulation strategy . . . . .	43
4.3	Materials used for the experimental simulations . . . . .	44
4.4	ROC curves: (a) aluminum-painted sandpaper; (b) black aluminum disk; (c) black plastic box . . . . .	45
4.5	ROC curves with complete knowledge of $\mathbf{L}_\downarrow$ : (a) aluminum-painted sandpaper; (b) black aluminum disk; (c) black plastic box . . . . .	46
4.6	ROC curves (TASI-600 sensor): (a) aluminum-painted sandpaper; (b) black aluminum disk; (c) black plastic box . . . . .	48

---

---

# List of Tables

---

- 2.1 Parameters used for the atmosphere simulation . . . . . 17
- 3.1 RE% for  $\hat{\alpha}_M$  and  $\hat{\epsilon}$  . . . . . 36
- 4.1 Probabilities of detection for the three materials, in case of known and estimated downwelling radiance, for two case studies: NEDT = 0.1K and  $P_{FA} = 10^{-3}$ , and NEDT = 0.2K and  $P_{FA} = 10^{-2}$  47

---

---

## Formation Activities during the Years of PhD Program

---

### First Year

- PhD+ 2017: *Valorizzazione della Ricerca, Innovazione, Spirito Imprenditoriale* - 5 credits
- L. Sanguinetti, UniPi: *Massive MIMO - Fundamentals and State-of-the-Art* - 4 credits
- M. Morelli, STMicroelectronics: *Semiconductor trip: from a simple idea to a complex manufacturing* - 6 credits
- L. Daniel, MIT: *Introduction to modeling and simulation of complex and multi-disciplinary dynamical systems* - 5 credits
- G. Coro, CNR: *Using e-Infrastructures for Biodiversity Conservation* - 5 credits
- J. Spataro, UniPi: *Academic Writing and Presentation Skills for Engineering PhD Students* - 4 credits

### Second Year

- J. Spataro, Unipi: *Academic Writing and Presentation Skills: Advanced Course (C1+)* - 5 credits
- G. Cola, UniPi: *Continuous Monitoring of Health and Well-Being using Wearable Sensors* - 3 credits

Total CFU: 37

---

---

## Biography

---

**Matteo Moscadelli** was born in San Miniato (Pisa, Italy) on August 26th, 1990. He received both the B.Sc. and the M.Sc. degree (*cum laude*) in Telecommunications Engineering (curriculum: *remote sensing signal processing*) from the University of Pisa, Italy, in 2013 and 2016, respectively. From October 2015 to April 2016 he was with the Passive Radar and Anti-Jamming Techniques Department at the Fraunhofer Institute for High Frequency Physics and Radar Techniques FHR, Wachtberg (Bonn), Germany. He investigated the utilization of satellite broadcast signals, such as DVB-S and DVB-S2, as illuminator of opportunity for passive radar imaging techniques like SAR or ISAR. He is currently a PhD candidate in Information Engineering under the supervision of Prof. Marco Diani and Prof. Giovanni Corsini at the Department of Information Engineering, Pisa, Italy. During his PhD he was a visiting researcher with the Imagers group of Leonardo Spa - Electronics Division, Campi Bisenzio, Firenze, Italy. He was involved in the design and development of a new MWIR-LWIR hyperspectral sensor. His research interests include radar and hyperspectral signal processing. Currently, he is a system engineer with the Imagers group of Leonardo Spa - Electronics Division, where he is involved in the design, development, and test of visible and infrared imaging sensors for surveillance purposes.

